Original Article

Author for correspondence:
Satabdi Das,
Email: satabdi.jugeol@gmail.com

CAMBRIDGE
UNIVERSITY PRESS

Petrogenesis of a nepheline syenite from parts of the Chotanagpur Granite Gneissic Complex: implications for Neoproterozoic crustal extension in the East Indian Shield

Satabdi Das[1] , Deepak K Sinha[2], Sanjoy Sanyal[1], Subrata Karmakar[1], Biswajit Panigrahi[3], Sirina Roy Choudhury[1], Shyamal Sengupta[1] and Pulak Sengupta[1]

[1]Department of Geological Sciences, Jadavpur University, Kolkata, 700032, India; [2]Atomic Minerals Directorate for Exploration and Research, Hyderabad, 500016, India and [3]Atomic Minerals Directorate for Exploration and Research, Jamshedpur, 831002, India

Abstract

The North Purulia Shear Zone that dissects the granulite basement of the Chotanagpur Granite Gneissic Complex of the East Indian Shield exposes a deformed and metamorphosed nepheline syenite. The studied 'foid-monzosyenite' shows high abundances of large ion lithophile elements and high field strength elements with low abundances of compatible elements. Trace-element signatures show negative U, Th, Zr, Ti and Pb and positive Sr, Ba and Eu anomalies with respect to the primitive mantle. The chondrite-normalized diagram shows strongly fractionated rare earth element patterns ($(La/Lu)_N$ ~23–87). Geochemical fingerprints suggest that the basanitic protolith was formed by low-degree partial melting of garnet peridotite in the sub-continental lithospheric mantle. The enriched large ion lithophile, high field strength element and light rare earth element concentrations (relative to primitive mantle) can be explained by a mixed mantle source with components from a previously deformed alkaline rock/carbonatite. Geochemical data do not support any significant crustal contamination and suggest variable fractionation of clinopyroxene, ilmenite, titanite and apatite from the parental melt. Petrological data are consistent with the view that the nepheline syenite magma was emplaced in a rift setting with a minimum temperature of 800–900°C, low fO_2 conditions (below the fayalite–magnetite–quartz buffer) at a mid-crustal depth between 950 and 900 Ma. The continental rift zone, however, did not lead to the formation of an open ocean basin. Subsequently, the studied rock and its basement was deformed and metamorphosed in a continent–continent collisional setting at ~900 Ma. Combining information from the other Indian occurrences with this study, it is demonstrated that the deformed alkaline rocks and carbonatite are potentially valuable for tracing the birth and demise of the palaeo-supercontinents.

1. Introduction

Alkaline rocks with their distinct geochemical signatures and exotic mineralogy are considered to be an important proxy for unravelling the crust–mantle interaction over geological time (Bailey & Schairer, 1966; Bailey, 1974; Mitchell & Platt, 1978; Price *et al.* 1985; Platt & Woolley, 1986; Baker, 1987; Dawson, 1987; Edgar, 1987; Fitton, 1987; Menzies, 1987; Zhao *et al.* 1995; Woolley *et al.* 1996; Burke *et al.* 2003; Burke & Khan, 2006; Leelanandam *et al.* 2006; Upadhyay *et al.* 2006*a,b,c*; Upadhyay & Raith, 2006). Extant information demonstrates that alkaline rocks occur in practically all different tectonic settings, except the mid-oceanic ridges (Zhao *et al.* 1995). However, there exists a large debate on the petrogenetic processes that are involved in producing alkaline magmas in the mantle. Opinions on the genesis of alkaline magma primarily fall into either of two groups, namely (a) the derivation of alkaline magma from metasomatized mantle enriched in light rare earth elements (LREEs) and large ion lithophile elements (LILEs) (Dawson, 1987; Edgar, 1987) or (b) a low degree of partial melting of the mantle followed by crystal fractionation (Bowen, 1928; Baker, 1987). After reviewing the existing information and analysing a comprehensive catalogue of the alkaline rocks of Africa, Woolley, (2001) opined that alkaline rocks are commonly associated with rifted continental margins. Burke *et al.* (2003) adopted a novel approach to trace the location of continental suture zones using deformed alkaline rocks with or without carbonatite (DARs/DARCs). The central theme of the concept seems to originate from the idea that alkaline rocks of the continents are produced in a rift region (extension-dominated process) eventually leading to the formation of an ocean basin. Subsequently, a compression leads to consumption of the oceanic crust and

reunites the previously fragmented continental blocks in a continent–continent collision. This latter concept has been supported by many studies (Leelanandam *et al.* 2006; Upadhyay & Raith, 2006; Upadhyay *et al.* 2006b,c; Upadhyay, 2008; Ashwal *et al.* 2016; Ranjan *et al.* 2018; Burke *et al.* 2007, 2008), though opinions to the contrary are also published (Upadhyay *et al.* 2006a; Das *et al.* 2019). Nevertheless, the studies of Woolley (2001) and Burke *et al.* (2003) provide a geodynamic context for the study of DARs/DARCs.

The Chotanagpur Granite Gneissic Complex (CGGC) is traversed by two prominent shear zones. These are (a) the South Purulia Shear Zone (SPSZ) that separates the CGGC from the North Singhbhum Fold Belt of the Singhbhum Craton (Fig. 1) and (b) the North Purulia Shear Zone (NPSZ) that runs through the south-central part of the CGGC (Fig. 1). Both the SPSZ and NPSZ contain occurrences of deformed nepheline syenites and carbonatites (DARCs; Goswami & Bhattacharyya, 2008; Chakrabarty & Sen, 2010; Goswami & Basu, 2013; Das *et al.* 2017, 2019). However, limited precise petrological and geochemical data are available on the deformed nepheline syenites of the NPSZ (reviewed in Das *et al.* 2019). Lack of a quality database renders determination of the petrogenesis and geodynamic setting of the intrusion (and subsequent modification) of this important rock type, difficult.

In this communication, we present field observations and detailed mineralogical and geochemical data of a deformed nepheline syenite from the Kusumdih area of the NPSZ. Integrating all the geological information it is proposed that the magmatic protolith of the studied rock was derived from low-degree partial melting of the subcontinental lithospheric mantle (SCLM) that lay beneath the ~950 Ma crust of the CGGC. The alkaline magma thus generated underwent fractional crystallization with minimal crustal contamination and produced nepheline syenite that was emplaced in a 'failed' rift zone/aulacogen within a time span of ~950–900 Ma. The geological features of the CGGC support the view that the rift setting in which the magmatic protolith of the studied rock was formed did not evolve into an open ocean basin. A change of tectonic polarity from an extensional to a compressional regime converted the nepheline syenite and the adjoining carbonatite to DARC at ~900 Ma. Along with the information from the DARs/DARCs, it is proposed that the evolutionary history of the DARs/DARCs can trace the formation and destruction of the ancient supercontinents.

2. Geological background

The study area is a high-grade metamorphic terrane near Saltora, Bankura, which is part of an E–W- to ENE–WSW-trending and very steeply northerly dipping discontinuous crustal-scale high-strain zone, the NPSZ (Goswami & Bhattacharyya, 2010; Karmakar *et al.* 2011; Das *et al.* 2019). The NPSZ lies in the southern portion of the CGGC, a Proterozoic sub-arcuate belt of the East Indian Shield (Fig. 1; Mahadevan, 2002; Acharyya, 2003; Sanyal & Sengupta, 2012; Mukherjee *et al.* 2019b). Exposed over an area of *c.* 80 000 km^2 in an E–W extent, the CGGC dominantly consists of orthogneisses, migmatites and granites (porphyritic and massive variety), along with metapelitic, calc-silicate and metabasic granulite enclaves and some intrusive rocks (Karmakar *et al.* 2011; Sanyal & Sengupta, 2012; Das *et al.* 2017, 2019; Mukherjee *et al.* 2019b; Dey *et al.* 2019a,b). E–W-trending northerly dipping shear foliation is the most dominant fabric in this tectonic zone (Goswami & Bhattacharyya, 2010; Mukherjee *et al.* 2019b).

Owing to complex structural patterns and metamorphic overprinting, the CGGC is recognized as a polydeformed and polymetamorphosed terrane that experienced three major tectonothermal events (M$_1$–M$_3$), recorded in the enclave suite of rocks, host granites and intrusive rocks (Maji *et al.* 2008; Sanyal & Sengupta, 2012; Mukherjee *et al.* 2019b; Das *et al.* 2019). The earliest deformation-metamorphism (M$_1$) is well constrained from the metapelitic enclaves and represented by high-temperature (HT: >850°C) to ultra-high-temperature and moderate-pressure conditions at ~1650 Ma (Sanyal & Sengupta, 2012; Dey *et al.* 2017, 2019b). M$_2$ is the most pervasive metamorphic event affecting the CGGC, evident from different lithological units including the host felsic orthogneisses that occurred under high-pressure granulite-grade conditions at 1100–950 Ma (Maji *et al.* 2008; Chatterjee *et al.* 2010; Karmakar *et al.* 2011; Chatterjee & Ghose, 2011; Rekha *et al.* 2011; Mukherjee *et al.* 2017, 2019a; Dey *et al.* 2019c). The latest one (M$_3$) is an amphibolite-grade metamorphic event documented from the alkaline rocks and mafic dykes intruding the felsic orthogneiss basement, and took place between ~920 and 780 Ma (Chatterjee *et al.* 2010; Sanyal & Sengupta, 2012; Mukherjee *et al.* 2018b; Das *et al.* 2019). Among the three major deformational events (D$_1$, D$_2$ and D$_3$) reported in this area, the earliest granulite-facies fabric S$_1$ is isoclinally folded to form the S$_2$ fabric, which together refolded into a set of E–W-closing non-cylindrical D$_3$ folds (Maji *et al.* 2008; Rekha *et al.* 2011). S$_3$ is the regionally pervasive E–W-trending northerly dipping foliation of the area, defined by an assemblage of biotite ± amphibole. It is a product of syn-shearing metamorphic recrystallization (M$_3$) and has transposed all the earlier fabrics (Karmakar *et al.* 2011; Das *et al.* 2019). The interlude period between the D$_2$ and D$_3$ deformations is marked by the intrusion of the alkaline rocks, carbonatite and mafic dykes (Sanyal & Sengupta, 2012; Das *et al.* 2017, 2019; Mukherjee *et al.* 2018b, 2019b). The alkaline rocks including the nepheline syenite of the Kankarkiari–Santuri area are likely to have been emplaced in the time span of ~950–900 Ma (Das *et al.* 2019). Similar alkaline magmatism has been reported from the southern contact of the CGGC with the SPSZ (intrusion age ~922 Ma; Fig. 1; Basu, 1993, 2003; Acharyya *et al.* 2006; Reddy *et al.* 2009; Chakrabarty & Sen, 2010; Goswami & Basu, 2013; Chakrabarty *et al.* 2016; Olierook *et al.* 2019).

3. Field relationships

Kusumdih village of Purulia (23.5544° N, 86.8793° E) (Bhaumik *et al.* 1990; Goswami & Bhattacharyya, 2008) exposes a hillock of nepheline syenite in an expanse of felsic orthogneisses (FOG). It is situated close to the Purulia–Bankura district boundary (in Domain-IA of the CGGC, according to the divisions of Mukherjee *et al.* 2019b; Fig. 1), ~8 km NW of Saltora town. It occurs as a contiguous but spatially discontinuous body with the nepheline syenite of Kankarkiari following an almost E–W trend (Fig. 2). Enclaves of khondalite of variable dimensions (a few centimetres to kilometre scale) are scattered randomly within the FOG. The nepheline syenite and mafic dykes are among the younger units of the study area that have intruded this felsic crust by cross-cutting the granulite-grade planar fabric S$_2$ (Das *et al.* 2019). S$_3$ is the E–W-trending amphibolite-grade mylonitic fabric that developed in the host FOG as well as in the alkaline rocks and is defined by oriented recrystallized grains of amphibole and biotite.

Khondalites are gneissic rocks with alternate bands of greyish white leucosome and dark brown melanosome layers. Leucosomal bands are mainly composed of quartzo-feldspathic minerals heavily
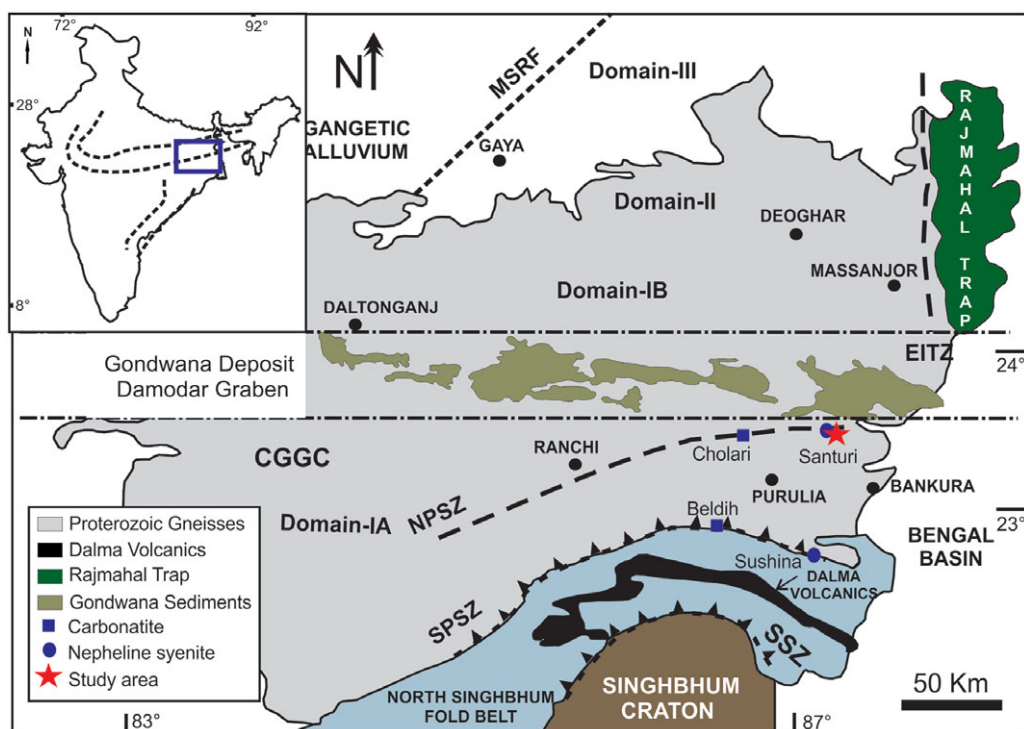
Fig. 1. (Colour online) General geological map of the East Indian Shield comprising the Chotanagpur Granite Gneissic Complex (CGGC) in the north, North Singhbhum Fold Belt (NSFB) in the middle and Singhbhum Craton in the south (modified after Acharyya, 2003). The red star shows the occurrence of the studied nepheline syenite in the southern portion of the Domain-IA of the CGGC. MSRF – Monghyr-Saharsa Ridge Fault; EITZ – Eastern Indian Tectonic Zone; NPSZ – North Purulia Shear Zone; SPSZ – South Purulia Shear Zone; SSZ – Singhbhum Shear Zone. Deformed nepheline syenites and carbonatites of the CGGC are marked as blue coloured circles and squares, respectively.

Fig. 2. (Colour online) Simplified litho-structural map showing distribution of alkaline rocks and associated rocks in and around Kankarkiari–Kusumdih village (modified after Das et al. 2019). The sample locations are indicated in white.

Fig. 3. (Colour online) (a) S₂ gneissic banding of the host felsic orthogneiss (FOG) swerving around the enclaves of khondalite. S₁ foliation of the khondalite enclave abuts against the external S₂ foliation at a high angle. (b) Greas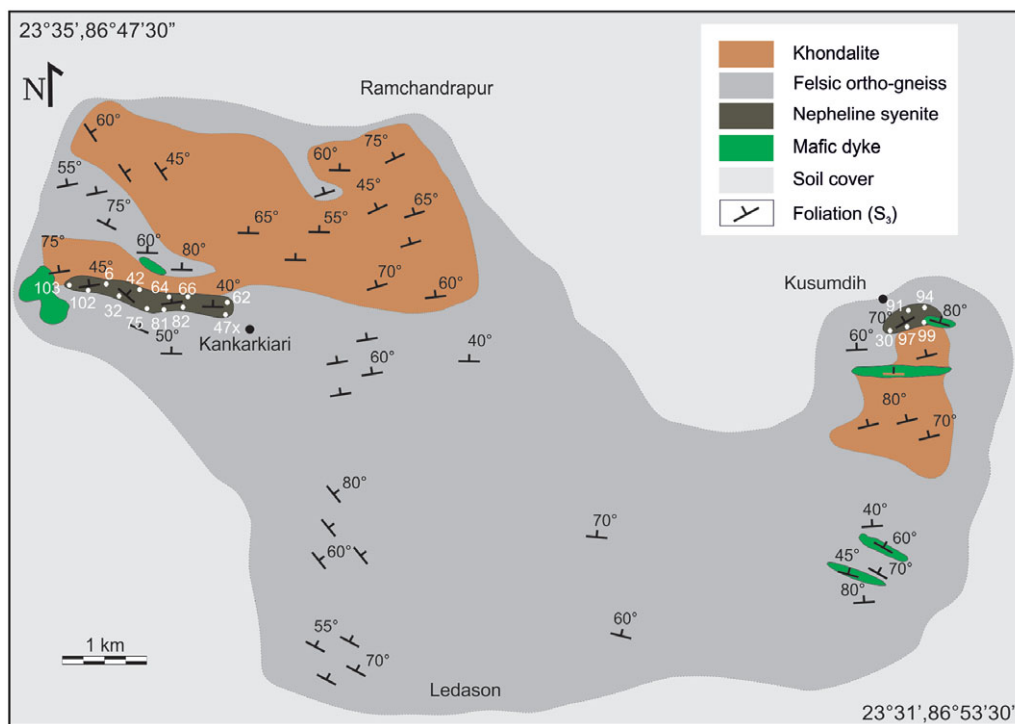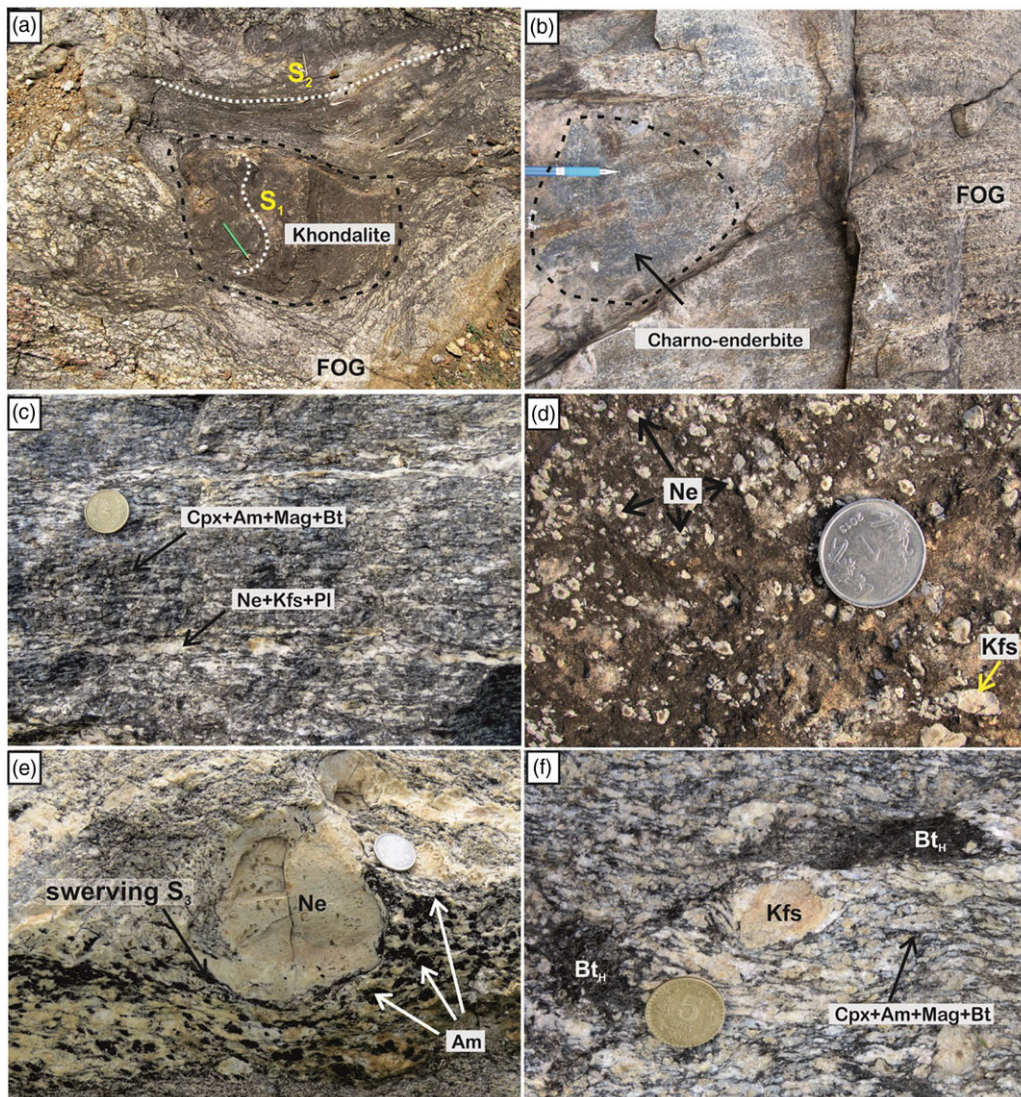y-looking charno-enderbite occurring as a patch in FOG, but with a gradational boundary; continuous S₂ foliation can be traced across the boundaries of the two units. (c) Gneissic foliation (S₃) in nepheline syenite defined by alternate thin dark, impersistent bands composed of biotite, amphibole and pyroxene and light grey coloured feldspars and nepheline. (d) Megacrystic nepheline and alkali feldspar sprinkled inhomogeneously within a fine-grained groundmass of nepheline-feldspar define relict porphyritic appearance of the rock. (e) The S₃ gneissic foliation defined by amphibole and/or biotite is swerving around nepheline porphyroclasts. (f) Secondary shear fabric composed of haphazard biotite grains in the rock.

sprinkled with reddish brown coloured garnet grains. Melanosome layers contain garnet, sillimanite and biotite. Migmatitic foliation of the FOG (S₂) swerves around the enclaves. Migmatitic foliation of the khondalitic enclaves (S₁) abuts against the S₂ foliation at a high angle and is dragged to parallelism at the contact (Fig. 3a). The FOG shows a migmatitic structure defined by thin to thick leucosomal bands composed mainly of plagioclase and quartz with a subordinate amount of K-feldspar that forms laterally continuous stromatic bands and/or nebular segregations. Melanosomes occur as impersistent dark segregates composed of fine-grained pyroxene, biotite and/or amphibole with occasional garnet. The FOG is interpreted to be retrogressed charno-enderbitic rock as greasy-looking rare patches of the latter occur within the FOG. Additionally, unlike the enclave suite of rocks, these charno-enderbitic patches share a gradational contact and continuous foliation with the host FOG (Fig. 3b). The nepheline syenite of Kusumdih is a dark grey coloured banded rock, completely devoid of quartz. The prominent gneissic banding in the rock is

defined by alternate thin, dark, impersistent bands composed of clinopyroxene, amphibole, biotite and magnetite and light bands composed of feldspar and nepheline (Fig. 3c). The grain size of the minerals and mafic content varies from layer to layer providing the rock with an inhomogeneous appearance. Relict porphyritic texture is occasionally preserved in locales with less intense deformation where megacrystic nepheline and K-feldspar grains are set in a finer grained groundmass composed of nepheline and feldspar (Fig. 3d). The S₃ foliation swerves past these megacrystic nephelines (Fig. 3e). Locally medium- to fine-grained biotite flakes form randomly oriented clusters suggesting their growth outlasted S₃ fabric development (Fig. 3f).

4. Petrographic description

The nepheline syenite of the studied area is a fine- (>0.5 mm diameter) to medium-grained (<4 mm diameter) rock composed of
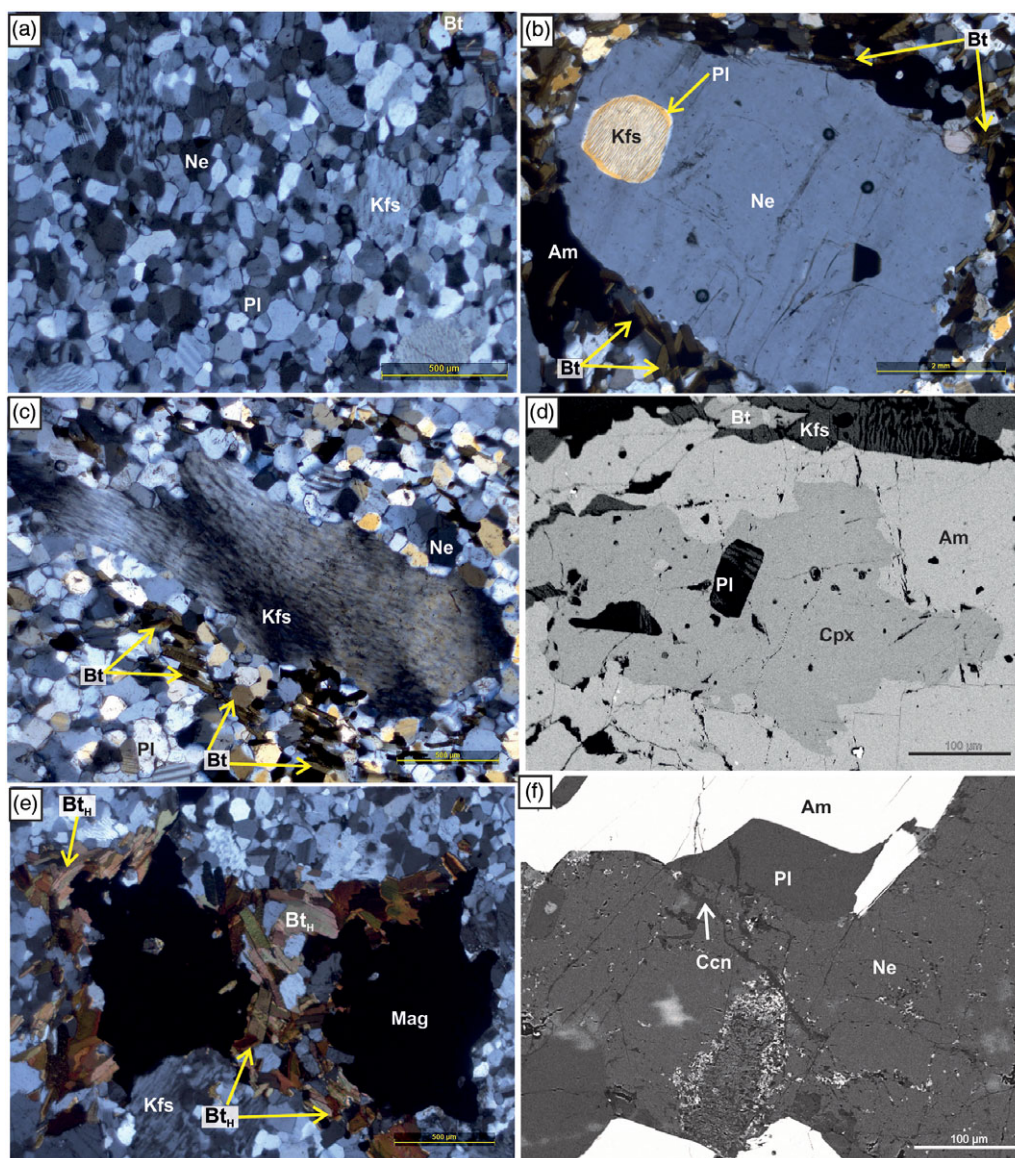
Fig. 4. (Colour online) (a) Intense deformation modified the pristine orthocumulus texture and developed a granoblastic mosaic of fine recrystallized nepheline (Ne), alkali feldspar (Kfs), plagioclase (Pl), clinopyroxene, magnetite, titanite, apatite and calcite grains with polygonal grain margins. (b) S_3 foliation defined by oriented grains of biotite (Bt) and amphibole (Am) swerves past spindle-shaped megacrystic nepheline; perthite with an albite rim occurs as an inclusion within the porphyroclast. (c) Lenticular megacrystic perthite records undulose extinction, bending of lamellae, marginal recrystallization and a core–mantle texture. (d) Back-scattered electron image shows oriented grains of amphibole and biotite replacing the magmatic phases (clinopyroxene (Cpx), plagioclase) as a result of metamorphism. (e) Randomly oriented biotite replaces ilmenite (Ilm), magnetite (Mag) and alkali feldspar along the margins. (f) Cancrinite (Ccn) veinlets replace nepheline grains along the fractures and cleavage planes.

feldspars (both K-feldspar and plagioclase), nepheline, clinopyroxene, amphibole, biotite and magnetite. Calcite, apatite, titanite, ilmenite, cancrinite, zeolite and zircon occur as accessory minerals. The modal content of nepheline varies greatly among the samples (10–35 vol. %); however, nepheline and feldspar constitute ~50–90 vol. % of the rock. The rock rarely preserves its pristine orthocumulus texture with a local porphyritic appearance. Commonly the rock has a matrix that is composed of fine-grained polygonal aggregates of nepheline, K-feldspar (perthite) and plagioclase in which porphyroclasts of nepheline, K-feldspar (perthite), clinopyroxene and magnetite occur as islands (Fig. 4a, b). The porphyroclasts bear the impression of crystal-plastic deformation, namely undulatory extinction, bending of mineral cleavage traces, stretching of grains with wedge-shaped deformation twin lamellae (in plagioclase) and the formation of sub-grains in feldspars and nepheline (Fig. 4c). Grain boundary recrystallization

of K-feldspar, plagioclase and nepheline forms a core–mantle texture (Fig. 4c). A few nepheline porphyroclasts include grains of perthite (Fig. 4b). The proportion of matrix minerals and porphyroclasts is variable even within a metre scale. Other than recrystallized polygonal grains in the matrix, plagioclase feldspar also occurs as granular exsolutions (thin to thick) around perthitic K-feldspar (Fig. 4b, c). Calcite, apatite, titanite and ilmenite occur as polygonal grains in the matrix. Exsolution lamellae of ilmenite are also observed within magnetite. Euhedral zircon grains are very fine in size (0.02–0.03 mm) and variable in modal abundance (mostly less than 5 vol. %). Thin-sections prepared from different layers throughout the whole nepheline syenite body are consistent with the variable modal proportions of amphibole and biotite, as evidenced from field observations. Clinopyroxene, mostly pseudomorphed by amphibole, only occurs as large to small undigested patches within the latter (Fig. 4d).

Amphibole and biotite variably replace other pristine phases like magnetite, titanite, feldspars and nepheline, both in the porphyroclastic as well as the matrix modes (Fig. 4d, e).

Ovoid, lenticular to spindle-shaped megacrystic nepheline and K-feldspar (perthite) phenocrysts with swerving oriented grains of biotite and/or amphibole appear to define a blasto-porphyritic texture set within the recrystallized matrix (Fig. 4b, c). Amphibole and biotite that grew along the S_3 fabric of the rock are considered to be the product of metamorphism (Fig. 4b). Biotite occurs in two textural modes: (a) fine-grained flakes oriented along the foliation plane, sometimes showing internal strain (Fig. 4b, c), and (b) medium-grained random flakes replacing magnetite, ilmenite, titanite and K-feldspar along the grain margin (Bt_H; Fig. 4e). The random orientation of the biotite suggests that its growth outlasted the deformation. Cancrinite, analcite and kaolinite are the alteration phases of nepheline that occur as patches or fine veinlets within nepheline (Fig. 4f). On the basis of textural features, the following sequence of mineral associations are noted:

- Relict igneous phases: nepheline, K-feldspar, plagioclase, clinopyroxene, magnetite, calcite, apatite, titanite and ilmenite.
- Metamorphic phases: amphibole and biotite.
- Low-temperature alteration phases: cancrinite, analcite and kaolinite.

5. Analytical techniques

The chemical composition of mineral phases was measured using a CAMECA SX5 microprobe at the Central Research Facility of the Indian Institute of Technology (Indian School of Mines), Dhanbad, India. For analysis, a 15 kV accelerating voltage and 15 nA beam current, with a beam diameter of ~1–2 μm was used for all the points. Well-characterized, natural and synthetic compounds were used as standards to calibrate the instruments for the analyses and the raw analyses were corrected with the PAP technique (Pouchou & Pichoir, 1984). Tabular rock samples (each at least 3 kg in weight) were used to prepare rock-powder for geochemical analyses. Bulk-rock analyses were carried out in the X-Ray Fluorescence laboratory of the National Centre for Earth Science Studies (NCESS), Thiruvananthapuram, Kerala, India. Major-element abundances were analysed by X-ray fluorescence on fused discs using a Bruker model S4 Pioneer sequential wavelength-dispersive X-ray spectrometer. Fused glass discs were prepared by fusing 1 g of finely powdered sample mixed with 5 g of lithium tetra-metaborate flux in a platinum crucible at 1100°C using a Claisse Fluxer. The analytical calibration lines used in the quantification program were produced by bivariate regression of data from certified geochemical reference materials encompassing a wide range of felsic rock compositions. The detection limit of major elements was ~0.01 %, and analytical precision is always better than 1 %. Precision for trace elements is estimated to be better than 5 % on the basis of repeated analysis of reference rock standards. Standards used for the analyses were G2, GSP2, STM1, SARM1, SARM2, SY3, RGM, GA, GH, GS-N, AC-E, MDOG, ISHG, VS-N, JG-1, JG-2, JG-3, JR-3 and JSY-1. The rare earth element (REE) and trace-element concentration analyses were performed at the Department of Earth Sciences, Indian Institute of Technology, Kanpur, using an Agilent triple quadrupole inductively coupled plasma mass spectrometer (QQQ-ICP-MS) following a collision/reaction technology. Collision cell technology together with MS/MS mode was used to remove spectral interferences. For trace-element analysis, ~0.5 g of dust laden filters were digested in

pre-cleaned Teflon beakers at 130 ± 5°C using a 3:1 mixture of HF and HNO_3 for 48 hours. After digestion, the samples were dried and re-dissolved in 1 ml of concentrated HNO_3. The acid was then slowly evaporated at 80 ± 5°C, and again, the samples were re-dissolved in 3 ml of Aqua Regia acid (concentrated HNO_3 and concentrated HCl in 2:1 ratio). Aqua Regia was fluxed for 24 hours. After the Aqua Regia digestion step, the samples were dried and re-dissolved in 2 % HNO_3. The acid digestion steps were only repeated when digestion was incomplete. Six procedural blanks and certified reference materials SBC-1 and AGV-2 were also digested following the same procedures. The blanks were analysed to quantify the total procedural blank, whereas the reference materials were analysed to assess the data quality. Concentrations were determined using a multi-element standard solution (High Purity Standard) diluted to seven appropriate concentrations depending on the signal range of the measured isotope. Added to the samples were 5 ng g^{-1} of high purity rhodium (Rh) standard as an internal standard, and monitored to assess matrix effects. The instrument was run both in no gas mode and helium gas mode to optimize the separation of measured isotopes from isobaric polyatomic interferences. The final concentrations were blank corrected using the average procedural blank concentrations, and the matrix effect was corrected by Rh normalization. All the elements agreed well with their certified values.

6. Results

6.a. Mineral compositions

Representative analyses of different minerals present in the studied rock are given in Tables 1–7. Abbreviations for the mineral names in the figures and tables have been used after Kretz (1983). The following section describes salient compositional characteristics of the different minerals.

6.a.1. Clinopyroxene

On the acmite–jadeite–quadrilateral pyroxene triangular diagram (Morimoto, 1988), the compositions of the clinopyroxene are plotted in the quadrilateral pyroxene field forming a continuous array close to the Ac–Q line (Fig. 5a; Table 1). The clinopyroxene is dominated by diopside and hedenbergite molecules (Quad >1.45 mol %) with significant non-quad components including jadeite (0.04–0.1 mol %), aegirine (0.07–0.18 mol %) and Al-tschermakite (0.04–0.07 mol %). X_{Mg} (= Mg/Mg + Fe^{2+}) of the clinopyroxene varies between 0.34 and 0.59 with low tetrahedral Al (up to 0.07 atoms per formula unit (apfu)). No significant compositional zoning in terms of X_{Mg} was noted in individual grains; however, bigger grains of clinopyroxene (X_{Mg} = 0.34–0.40, in sample no. NP42A) are less magnesian compared to the smaller ones (X_{Mg} = 0.56–0.59, in sample no. NP47X). On the Na/(Na + Ca) versus $Al_{VI}/(Al_{VI} + Fe^{3+})$ diagram, the pyroxene compositions straddle the boundary between diopside–hedenbergite and aegirine–augite (Fig. 5b). The Na/(Na + Ca) ratio shows a negative correlation with $Al_{VI}/(Al_{VI} + Fe^{3+})$ suggesting jadeiitic substitution, presumably during metamorphism (Woolley *et al.* 1996; Upadhyay *et al.* 2006c).

6.a.2. Amphibole

According to the classification scheme of Leake *et al.* (1997), the amphibole compositions of the studied rock fall in the field of ferro-pargasite to hastingsite of the low Ti (Ti <0.5) calcic group (Fig. 5c; Table 2). X_{Mg} of amphibole varies within a restricted

Table 1. Representative oxide analyses (wt %) and calculated cations per formula unit of clinopyroxene

Phase	Clinopyroxene												
Sample no.	NP42A									NP47X			
Dataset	19	21	30	48	51	52	42	44	69	91	95	98	99
Position	rim	core	core	rim	core	rim				inclusion in Am			
SiO$_2$	49.43	48.61	49.56	49.90	50.18	49.93	49.59	49.49	49.63	49.37	50.40	49.67	49.98
TiO$_2$	0.81	0.82	0.98	0.63	0.65	0.67	0.76	0.82	0.66	1.13	0.98	1.09	1.27
Al$_2$O$_3$	3.69	3.59	4.21	3.20	3.64	3.11	3.51	3.80	3.71	4.23	4.36	4.32	4.25
FeO$_t$	18.14	19.39	18.53	18.40	18.48	18.51	18.60	18.42	18.54	13.10	13.43	13.35	12.89
MnO	0.51	0.53	0.49	0.45	0.46	0.47	0.62	0.53	0.54	0.42	0.44	0.50	0.35
MgO	4.78	4.47	5.12	5.01	4.95	5.15	4.87	4.85	4.87	7.53	7.59	7.49	7.83
CaO	18.35	19.14	18.25	18.25	18.43	18.29	18.16	18.00	18.29	20.45	19.87	20.17	19.98
Na$_2$O	2.95	2.20	2.31	2.94	3.16	2.91	2.99	3.16	3.11	2.31	2.43	2.33	2.26
K$_2$O	0.02	0.00	0.01	0.02	0.00	0.00	0.01	0.00	0.01	0.05	0.01	0.00	0.00
P$_2$O$_5$	0.01	0.00	0.00	0.03	0.00	0.07	0.04	0.00	0.06	0.00	0.00	0.05	0.00
Total	98.69	98.75	99.46	98.83	99.95	99.11	99.15	99.02	99.42	98.58	99.48	98.97	98.81
6 oxygen basis													
Si	1.929	1.915	1.930	1.940	1.930	1.940	1.928	1.920	1.921	1.900	1.920	1.902	1.913
Ti	0.024	0.024	0.030	0.020	0.020	0.020	0.022	0.024	0.019	0.030	0.030	0.031	0.037
Al	0.170	0.167	0.190	0.150	0.160	0.140	0.161	0.174	0.169	0.190	0.200	0.195	0.192
Fe^{3+}	0.150	0.124	0.070	0.150	0.180	0.160	0.165	0.175	0.185	0.130	0.100	0.111	0.076
Fe^{2+}	0.442	0.515	0.530	0.450	0.420	0.450	0.439	0.422	0.415	0.290	0.330	0.316	0.337
Mn	0.017	0.018	0.020	0.010	0.010	0.020	0.020	0.017	0.018	0.010	0.010	0.016	0.011
Mg	0.278	0.262	0.300	0.290	0.280	0.300	0.282	0.281	0.281	0.430	0.430	0.428	0.447
Ca	0.767	0.808	0.760	0.760	0.760	0.760	0.756	0.748	0.758	0.840	0.810	0.828	0.820
Na	0.223	0.168	0.170	0.220	0.240	0.220	0.225	0.238	0.233	0.170	0.180	0.173	0.168
K	0.001	0.000	0.000	0.000	0.000	0.000	0.000	0.000	0.000	0.000	0.000	0.000	0.000
Total	4.000	4.000	4.000	4.000	4.000	4.000	4.000	4.000	4.000	4.000	4.000	4.000	4.000
Al$_{IV}$	0.048	0.061	0.040	0.040	0.050	0.040	0.050	0.056	0.060	0.070	0.060	0.067	0.050
Al$_{VI}$	0.122	0.105	0.150	0.110	0.110	0.100	0.111	0.118	0.109	0.120	0.140	0.128	0.142
Wo (Ca/Ca + Fe^{2+} + Mg)	0.767	0.808	0.760	0.760	0.760	0.760	0.756	0.748	0.758	0.840	0.810	0.828	0.820
En (Mg/Ca + Fe^{2+} + Mg)	0.278	0.262	0.300	0.290	0.280	0.300	0.282	0.281	0.281	0.430	0.430	0.428	0.447
Fs (Fe^{2+}/Ca + Fe^{2+} + Mg)	0.442	0.515	0.530	0.450	0.420	0.450	0.439	0.422	0.415	0.290	0.330	0.316	0.337
Ac (if (Na > Jd, Na-Jd, 0))	0.150	0.124	0.070	0.150	0.180	0.160	0.165	0.175	0.185	0.130	0.100	0.111	0.076
Jd (if (Al$_{VI}$ > Na, Na, 0))	0.073	0.044	0.100	0.070	0.060	0.060	0.060	0.062	0.048	0.040	0.080	0.062	0.092
Al$_{Ts}$ (if (Al$_{VI}$ > Jd, Al$_{VI}$-Jd, 0))	0.049	0.061	0.040	0.040	0.050	0.040	0.051	0.056	0.061	0.070	0.060	0.067	0.050
Q (Ca + Fe^{2+} + Mg)	1.487	1.585	1.590	1.500	1.460	1.510	1.478	1.451	1.454	1.570	1.570	1.571	1.603
J (2Na)	0.446	0.336	0.350	0.440	0.470	0.440	0.451	0.475	0.467	0.340	0.360	0.346	0.336
X$_{Fe}$	0.614	0.662	0.639	0.608	0.600	0.600	0.609	0.601	0.596	0.410	0.440	0.425	0.430
X$_{Mg}$	0.386	0.338	0.361	0.392	0.400	0.400	0.391	0.399	0.404	0.590	0.560	0.575	0.570

Fe^{3+} recalculated on the basis of stoichiometry.
Zero stands for 'too low' values of oxides, measured by EPMA.

Table 2. Representative oxide analyses (wt %) and calculated cations per formula unit of amphibole

Phase	Amphibole											
Sample no.	NP42A						NP47X					
Name	Ferro-pargasite						Hastingsite					
Dataset	7	8	15	20	23	71	67	61	69	61	20	54
Position	adjacent to cpx			away from cpx			adjacent to cpx			away from cpx		
SiO_2	38.36	38.28	37.96	38.11	38.32	36.39	36.80	36.70	36.86	36.70	38.11	36.60
TiO_2	3.24	3.36	3.35	3.85	3.64	1.49	2.21	2.23	2.08	2.23	3.85	2.51
Al_2O_3	11.18	10.94	11.20	11.26	11.22	14.56	13.31	13.47	13.42	13.47	11.26	13.21
FeO_t	25.29	24.85	24.44	24.96	25.01	27.37	25.98	28.00	26.11	28.00	24.96	26.34
MnO	0.60	0.49	0.61	0.50	0.54	0.43	0.50	0.38	0.50	0.38	0.50	0.49
MgO	3.64	3.53	3.43	3.39	3.45	2.91	3.06	2.95	3.07	2.95	3.39	2.83
CaO	10.04	9.84	9.86	9.89	9.81	9.04	9.89	9.42	10.29	9.42	9.89	10.11
Na_2O	2.76	2.79	2.70	2.79	2.72	3.07	3.18	2.97	3.20	2.97	2.79	3.09
K_2O	1.88	1.91	1.93	1.90	1.88	2.72	2.26	2.39	2.19	2.39	1.90	2.27
P_2O_5	0.04	0.05	0.00	0.00	0.00	0.08	0.02	0.17	0.00	0.17	0.00	0.01
Total	97.02	96.04	95.42	96.65	96.59	98.07	97.24	98.68	97.72	98.77	96.61	97.47
23 oxygen basis												
Si	6.160	6.210	6.180	6.142	6.168	5.750	5.890	5.789	5.872	5.790	6.140	5.860
Al (IV)	1.840	1.790	1.820	1.858	1.832	2.250	2.110	2.211	2.128	2.210	1.860	2.140
Ti	0.000	0.000	0.000	0.000	0.000	0.000	0.000	0.000	0.000	0.000	0.000	0.000
Sum T	8.000	8.000	8.000	8.000	8.000	8.000	8.000	8.000	8.000	8.000	8.000	8.000
Al (VI)	0.270	0.300	0.340	0.281	0.297	0.460	0.400	0.294	0.392	0.290	0.280	0.350
Ti	0.390	0.410	0.410	0.467	0.441	0.180	0.270	0.265	0.249	0.260	0.470	0.300
Fe^{3+}	0.060	0.000	0.000	0.022	0.022	0.910	0.470	0.786	0.461	0.790	0.000	0.420
Mg	0.870	0.850	0.830	0.814	0.828	0.680	0.730	0.694	0.729	0.690	0.810	0.680
Fe^{2+}	3.330	3.380	3.350	3.386	3.345	2.700	3.000	2.908	3.017	2.910	3.390	3.100
Mn	0.070	0.070	0.080	0.068	0.067	0.060	0.070	0.043	0.067	0.040	0.070	0.070
Sum C	5.000	5.000	4.990	4.994	5.000	4.990	4.940	5.000	4.916	5.000	4.990	4.930
Mg	0.000	0.000	0.000	0.000	0.000	0.000	0.000	0.000	0.000	0.000	0.000	0.000
Fe^{2+}	0.000	0.000	0.000	0.000	0.000	0.000	0.000	0.000	0.000	0.000	0.000	0.000
Mn	0.010	0.000	0.000	0.000	0.006	0.000	0.000	0.008	0.000	0.010	0.000	0.000
Ca	1.730	1.710	1.720	1.708	1.692	1.530	1.690	1.592	1.756	1.590	1.710	1.730
Na	0.260	0.290	0.280	0.292	0.302	0.470	0.310	0.400	0.244	0.400	0.290	0.270
Sum B	2.000	2.000	2.000	2.000	2.000	2.000	2.000	2.000	2.000	2.000	2.000	2.000
Ca	0.000	0.000	0.000	0.000	0.000	0.000	0.000	0.000	0.000	0.000	0.000	0.000
Na	0.600	0.590	0.570	0.580	0.547	0.470	0.680	0.509	0.745	0.510	0.580	0.690
K	0.390	0.400	0.400	0.391	0.386	0.550	0.460	0.481	0.445	0.480	0.390	0.460
Sum A	0.980	0.980	0.980	0.970	0.933	1.020	1.140	0.990	1.190	0.990	0.970	1.160
TOTAL	15.980	15.980	15.970	15.964	15.933	16.010	16.080	15.990	16.105	15.990	15.960	16.090
X_{Mg}	0.207	0.201	0.199	0.194	0.198	0.201	0.196	0.193	0.195	0.192	0.193	0.180

Fe^{3+} recalculated on the basis of stoichiometry.
Zero stands for 'too low' values of oxides, measured by EPMA.

Table 3. Representative oxide analyses (wt %) and calculated cations per formula unit of biotite

Phase	Biotite														
Dataset	55	24	15	18	24	45	47	16	14	39	5	11	49	43	26
Type	oriented										random				
Position	adjacent to Am								adjacent to Ilm, Ttn				adjacent to Kfs		
SiO_2	32.36	33.65	33.53	34.38	33.72	33.84	32.55	33.80	33.55	33.90	34.39	34.88	33.33	33.01	35.57
TiO_2	4.75	4.31	4.39	4.21	4.71	4.52	4.96	5.21	5.66	5.98	6.14	6.04	3.72	3.00	2.41
Al_2O_3	14.97	15.44	14.98	15.12	14.71	14.78	15.72	14.90	14.79	14.37	12.17	12.25	16.53	15.16	13.11
FeO_t	29.64	28.54	28.17	28.30	26.98	27.38	31.45	27.21	27.47	26.40	32.4	31.83	30.77	33.39	27.90
MnO	0.53	0.55	0.44	0.43	0.11	0.21	0.38	0.43	0.39	0.41	0.24	0.05	0.33	0.34	0.44
MgO	4.26	4.25	4.52	5.65	6.42	6.78	2.90	4.95	5.06	6.17	2.22	2.42	3.15	2.91	3.03
CaO	0.00	0.02	0.02	0.00	0.00	0.00	0.05	0.13	0.00	0.01	0.06	0.02	0.27	0.03	9.57
Na_2O	0.17	0.02	0.15	0.14	0.13	0.18	0.16	0.15	0.10	0.19	0.02	0.06	0.12	0.12	2.97
K_2O	9.96	9.08	8.92	9.38	9.77	9.56	9.56	8.78	9.16	9.58	8.76	8.67	9.41	9.36	2.46
P_2O_5	0.00	0.00	0.00	0.00	0.00	0.00	0.00	0.00	0.00	0.04	0.05	0	0.02	0.00	0.16
F	0.00	NA	NA	0.00	0.01	0.00	NA	NA	NA	0.00	NA	NA	0.02	NA	NA
Total	96.64	95.83	95.20	98.48	96.87	97.62	97.82	95.54	96.08	97.28	97.38	96.22	97.85	97.42	97.62
11 oxygen basis															
Si	2.636	2.764	2.770	2.749	2.710	2.697	2.649	2.776	2.740	2.724	2.889	2.927	2.698	2.698	2.838
Ti	0.291	0.266	0.273	0.253	0.285	0.271	0.304	0.322	0.348	0.362	0.388	0.381	0.227	0.184	0.145
Al	1.437	1.495	1.458	1.425	1.394	1.388	1.508	1.442	1.423	1.361	1.205	1.212	1.577	1.460	1.233
Fe^{3+}	0.000	0.000	0.000	0.000	0.000	0.000	0.000	0.000	0.000	0.000	0.000	0.000	0.000	0.000	0.000
Fe^{2+}	2.019	1.960	1.946	1.893	1.813	1.825	2.140	1.869	1.876	1.774	2.276	2.234	2.083	2.282	1.861
Mn	0.037	0.038	0.031	0.029	0.008	0.014	0.026	0.030	0.027	0.028	0.017	0.004	0.023	0.024	0.030
Mg	0.517	0.520	0.557	0.673	0.770	0.806	0.352	0.606	0.616	0.739	0.278	0.303	0.380	0.355	0.361
Ca	0.000	0.002	0.002	0.000	0.000	0.000	0.004	0.011	0.000	0.001	0.005	0.002	0.023	0.003	0.818
Na	0.027	0.003	0.024	0.021	0.021	0.028	0.025	0.024	0.016	0.030	0.003	0.010	0.019	0.019	0.459
K	1.035	0.951	0.940	0.957	1.001	0.972	0.992	0.920	0.954	0.982	0.939	0.928	0.972	0.976	0.251
Total	8.000	8.000	8.000	8.000	8.000	8.000	8.000	8.000	8.000	8.000	8.000	8.000	8.000	8.000	7.994
X_{Fe}	0.796	0.790	0.778	0.738	0.702	0.694	0.859	0.755	0.753	0.706	0.891	0.881	0.846	0.866	0.838
X_{Mg}	0.204	0.210	0.222	0.262	0.298	0.306	0.141	0.245	0.247	0.294	0.109	0.119	0.154	0.134	0.162

Fe^{3+} recalculated on the basis of stoichiometry.
Zero stands for 'too low' values of oxides, measured by EPMA, whereas NA values are not measured.

range of 0.18–0.21. Individual grains of amphibole do not show any significant compositional zoning. However, owing to Fe–Mg exchange between clinopyroxene and amphibole, amphibole grains at the contact of low-magnesian clinopyroxene show an increase in X_{Mg} (0.20–0.21).

6.a.3. Biotite
The biotite compositions vary with the textural type. Relatively smaller grains of biotite at the contact with amphibole that define the planar fabric are more magnesian (X_{Mg} = 0.20–0.31) than the relatively larger and randomly oriented biotite grains (nos. 49, 43 and 26 in Table 3) that replace K-feldspar, ilmenite and titanite (X_{Mg} up to 0.16). Domainal variation of biotite composition suggests that local equilibrium was achieved with restricted mass

transport during the overprinting metamorphism. TiO_2 contents of metamorphic biotite (adjacent to amphibole) are high (4.21–4.96 wt %, mean value 4.48 ± 0.2). A few grains replacing ilmenite or titanite have the highest values of TiO_2 contents (up to 6.14 wt %), while a few adjacent to K-feldspar have distinctly lower values of TiO_2 (2.41–3.72 wt %). High TiO_2 bearing biotite at the contact of TiO_2-rich minerals is common in metamorphic rocks (Sengupta *et al.* 1990).

6.a.4. Nepheline
Nepheline compositions (end-member components calculated after Deer *et al.* 1962) vary in range $Ne_{69.04–73.13}$ $Kls_{17.5–19.18}$ $Qtz_{7.14–10.63}$ $An_{1.09–1.38}$, and plotted in a single cluster on the normative nepheline–kalsilite–silica diagram (Fig. 5d;

Table 4. Representative oxide analyses (wt %) and calculated cations per formula unit of nepheline

Phase	Nepheline											
Dataset	2	3	7	8	9	13	15	19	36	38	44	45
Type	recrystallized				porphyroclasts							
Position	in matrix				core	rim	core	rim	core	rim	core	rim
SiO_2	43.51	43.54	44.09	43.76	43.76	43.79	43.20	43.67	43.81	43.98	43.94	43.45
Al_2O_3	33.81	34.01	33.90	33.92	33.82	33.57	33.60	33.95	35.01	34.11	34.56	34.35
CaO	0.53	0.52	0.53	0.53	0.56	0.54	0.44	0.44	0.49	0.55	0.46	0.51
Na_2O	16.22	16.42	16.17	16.23	16.18	16.25	16.17	16.34	15.60	16.14	16.03	15.89
K_2O	6.43	6.17	6.05	6.07	6.11	6.27	6.49	6.17	6.57	6.42	6.33	6.48
Total	100.63	100.74	100.84	100.71	100.50	100.43	100.08	100.87	101.64	101.41	101.47	100.84
4 oxygen basis												
Si	8.460	8.400	8.520	8.520	8.520	8.520	8.400	8.460	8.454	8.483	8.475	8.430
Al	7.740	7.740	7.740	7.740	7.740	7.680	7.740	7.740	7.962	7.754	7.856	7.855
Ca	0.120	0.120	0.120	0.120	0.120	0.120	0.120	0.120	0.101	0.114	0.095	0.106
Na	6.120	6.180	6.060	6.120	6.120	6.120	6.120	6.120	5.836	6.036	5.994	5.977
K	1.620	1.500	1.500	1.500	1.500	1.560	1.620	1.500	1.617	1.580	1.558	1.604
Total	24.000	24.000	24.000	24.000	24.000	24.000	24.000	23.940	24.000	24.000	24.000	24.000
Ne	72.280	73.130	71.090	71.900	71.670	71.940	72.600	72.560	69.040	71.153	70.733	70.906
Kls	18.840	18.070	17.500	17.690	17.800	18.260	19.180	18.020	19.132	18.623	18.378	19.026
Q	7.570	7.520	10.120	9.100	9.150	8.480	7.140	8.330	10.630	8.884	9.767	8.811
An	1.310	1.270	1.290	1.300	1.380	1.310	1.080	1.090	1.198	1.340	1.122	1.258
vacancy	1.020	1.020	1.010	1.010	1.010	1.030	1.020	1.010	0.949	0.997	0.973	0.979

Zero stands for 'too low' values of oxides, measured by EPMA.
Concentrations of Ti, Fe, Mn, Mg and P are too low, thereby not provided in the table.

Hamilton, 1961; Table 4). These nephelines mostly have an excess vacancy in the tetrahedral cation site $((Na + K + 2*Ca)/(Al + Fe^{3+}) \sim 1)$; Rossi *et al.* 1989). No significant compositional zoning was noted in the individual grains. Also, the compositions of porphyroclastic and matrix nephelines were found to be overlapping.

6.a.5. Feldspar

K-feldspar composition is $Or_{79–80}$ $Ab_{21–23}$ An_0 (Table 5). No compositional variation is noted between the large porphyroclastic and recrystallized varieties of K-feldspar. Plagioclase feldspar shows two compositional groups: (a) the porphyroclastic and the recrystallized polygonal plagioclase grains in the matrix are compositionally oligoclase ($Ab_{88–89}$ $An_{11–10}$) and (b) the plagioclase that occurs either as exsolved lamellae or fine veinlets within perthitic K-feldspar or forms a thin rim around K-feldspar and nepheline is albitic ($Ab_{97–99}$ $An_{3–1}$; Table 5).

6.a.6. Other phases

Apatite is fluorapatite with F-content ranging between 3.04 and 3.66 wt % (Table 6). The occurrence of fluorapatite in alkaline rocks and carbonatite is common in nature (Liferovich & Mitchell, 2006).

Magnetite contains up to 2.73 wt % TiO_2 (Table 7).
Ilmenite shows significant MnO (up to 5.39 wt %) (Table 7).
Titanite contains up to 1.4 wt % Al_2O_3 in its structure (Table 7).

Cancrinite, *calcite* (Table 7), *analcite* and *kaolinite* have nearly end-member compositions.

6.b. Major- and trace-element compositions

The representative analyses for whole-rock compositions of the studied rock are listed in Table 8. The following section presents the salient features of the major- and trace-element behaviour of the studied rock.

On the F(feldspathoid)–A(alkali feldspar)–P(plagioclase) diagram, most of the studied samples are plotted in the field of 'foid-monzosyenite'. Only a few data points are plotted in the field of 'foid-bearing monzonite' (Fig. 6a; Le Maitre, 2002). The studied samples show a higher concentration of total alkalis ($Na_2O + K_2O$ ~13 ± 3 wt %), with SiO_2 contents ranging between 44 and 57 wt % (~52 ± 4 wt %; ~54 ± 1.5 wt % excluding three samples with SiO_2 <50 wt %). On the Total Alkali Silica (TAS) diagram, the studied samples cluster in the field of 'nepheline syenite', excluding three data points that fall in the field between 'ijolite' and 'gabbro' (Fig. 6b; Le Bas *et al.* 1992). Except for one sample (NP94B), the average K_2O/Na_2O ratio of the studied rock is close to 1 (~1.4 ± 0.4, the odd sample has the ratio 3.65). On the K_2O versus SiO_2 diagram, all the samples are plotted in the 'shoshonitic' field (Fig. 6c; Peccerillo & Taylor, 1976). Owing to the high Al_2O_3 content (~21 ± 2 wt %) of the rock, the samples straddle between the fields of 'metaluminous' and 'peralkaline' rocks on the molar A/NK

Table 5. Representative oxide analyses (wt %) and calculated cations per formula unit of feldspars

Phase	Alkali feldspar						Plagioclase					
Dataset	6	10	11	12	5	20	89	43	49	53	69	78
Position	porphyroclast			in matrix			in matrix			granular exsolution		
SiO_2	65.48	64.32	64.56	65.50	65.52	65.28	66.08	65.82	66.10	67.93	67.66	66.02
Al_2O_3	18.90	18.59	19.03	18.73	18.57	18.43	21.74	21.41	21.63	20.19	20.22	21.09
CaO	0.00	0.00	0.02	0.00	0.00	0.00	2.26	2.34	2.03	0.60	0.52	0.19
Na_2O	2.13	1.59	1.78	2.33	2.48	2.23	9.61	9.97	10.10	10.68	10.79	12.14
K_2O	13.00	15.68	15.04	12.98	12.61	12.85	0.07	0.16	0.11	0.20	0.13	0.06
Total	99.65	100.26	100.43	99.91	99.33	98.98	99.81	99.75	100.12	99.71	99.57	99.60
8 oxygen basis												
Si	3.020	2.940	2.941	3.010	3.020	3.030	2.930	2.910	2.910	2.990	2.980	2.880
Al	1.030	1.002	1.022	1.010	1.010	1.010	1.140	1.120	1.120	1.050	1.050	1.080
Ca	0.000	0.000	0.001	0.000	0.000	0.000	0.110	0.110	0.100	0.030	0.020	0.010
Na	0.190	0.141	0.157	0.210	0.220	0.200	0.830	0.850	0.860	0.910	0.920	1.030
K	0.760	0.914	0.874	0.760	0.740	0.760	0.000	0.010	0.010	0.010	0.010	0.000
Total	5.000	4.997	4.995	5.000	5.000	5.000	5.000	5.000	5.000	5.000	5.000	5.000
An	0.000	0.000	0.001	0.000	0.000	0.000	0.110	0.110	0.100	0.030	0.030	0.010
Ab	0.200	0.134	0.152	0.210	0.230	0.210	0.880	0.880	0.890	0.960	0.970	0.990
Or	0.800	0.866	0.847	0.790	0.770	0.790	0.000	0.010	0.010	0.010	0.010	0.000

Zero stands for 'too low' values of oxides, measured by EPMA.
Concentrations of Ti, Fe, Mn, Mg and P are too low, thereby not provided in the table.

Table 6. Representative oxide analyses (wt %) and calculated cations per formula unit of apatite

Phase	Apatite												
Dataset	18	20	23	24	25	28	29	65	77	78	85	86	100
SiO_2	0.33	0.35	0.42	0.43	0.39	0.50	0.17	0.43	0.19	0.15	0.24	0.18	0.25
CaO	54.52	54.33	54.04	54.08	54.44	54.01	54.14	55.02	54.46	54.57	54.36	53.99	54.60
Na_2O	0.16	0.11	0.09	0.07	0.10	0.12	0.65	0.12	0.04	0.00	0.03	0.05	0.05
P_2O_5	42.71	41.54	41.98	42.49	41.88	41.75	42.46	41.65	41.88	43.19	42.76	41.97	41.88
Cl	0.06	0.07	0.07	0.06	0.01	0.07	0.01	0.01	0.04	0.06	0.05	0.07	0.05
F	3.64	3.53	3.45	3.36	3.38	3.30	3.50	3.66	3.28	3.58	3.62	3.54	3.04
Total	101.68	100.23	100.57	100.92	100.48	100.09	101.23	101.06	100.09	101.99	101.19	100.13	100.07
25 oxygen basis													
Si	0.053	0.057	0.068	0.070	0.064	0.082	0.028	0.070	0.031	0.024	0.039	0.029	0.041
Fe^{2+}	0.015	0.016	0.026	0.026	0.014	0.015	0.019	0.004	0.000	0.024	0.000	0.015	0.003
Ca	9.390	9.530	9.434	9.383	9.513	9.472	9.380	9.576	9.557	9.361	9.393	9.459	9.584
Na	0.050	0.035	0.028	0.022	0.032	0.038	0.203	0.038	0.013	0.000	0.009	0.016	0.016
P	5.812	5.758	5.791	5.826	5.783	5.786	5.813	5.728	5.808	5.854	5.838	5.810	5.809
Cl	0.016	0.019	0.019	0.016	0.003	0.019	0.003	0.003	0.011	0.016	0.014	0.019	0.014
F	1.850	1.828	1.778	1.721	1.743	1.708	1.790	1.880	1.699	1.813	1.846	1.831	1.575
Total	17.187	17.247	17.158	17.072	17.151	17.123	17.251	17.298	17.119	17.109	17.139	17.188	17.048

Zero stands for 'too low' values of oxides, measured by EPMA.
Concentrations of Ti, Al, Fe, Mn, Mg and K are too low, thereby not provided in the table.

Table 7. Representative oxide analyses (wt %) and calculated cations per formula unit of magnetite, ilmenite, titanite and calcite

Phase	Magnetite (4-O)		Ilmenite (3-O)		Titanite (5-O)		Calcite (1-O)	
Dataset	40	74	77	78	101	103	20	91
SiO_2	0.04	0.08	0.11	0.01	30.29	29.79	0.00	0.00
TiO_2	2.73	0.67	50.18	50.43	38.06	37.90	0.03	0.04
Al_2O_3	0.44	0.40	0.13	0.75	1.32	1.40	0.00	0.00
FeO_t	86.04	91.14	41.76	41.24	0.33	0.34	0.29	0.31
MnO	0.11	0.17	4.93	5.39	0.10	0.09	0.14	0.13
MgO	0.01	0.00	0.03	0.15	0.00	0.01	0.04	0.04
CaO	0.17	0.08	0.13	0.09	28.06	28.13	58.08	57.97
Na_2O	0.00	0.00	0.00	0.00	0.05	0.02	0.00	0.00
K_2O	0.02	0.03	0.01	0.00	0.00	0.01	0.00	0.00
P_2O_5	0.00	0.00	0.00	0.00	0.02	0.03	0.18	0.15
F	NA	NA	NA	NA	0.19	0.33	0.00	0.00
Total	89.52	92.53	97.28	98.06	98.92	98.53	58.77	58.64
Calculated cation								
Si	0.000	0.000	0.000	0.000	1.000	0.990	0.000	0.000
Ti	0.050	0.020	0.980	0.970	0.940	0.940	0.000	0.000
Al	0.010	0.020	0.000	0.020	0.050	0.050	0.000	0.000
Fe^{3+}	1.880	1.940	0.040	0.040	0.000	0.000	0.000	0.000
Fe^{2+}	1.010	1.010	0.870	0.850	0.010	0.010	0.000	0.010
Mn	0.000	0.010	0.110	0.120	0.000	0.000	0.000	0.000
Mg	0.000	0.000	0.000	0.010	0.000	0.000	0.000	0.000
Ca	0.000	0.000	0.000	0.000	0.990	1.000	0.990	0.990
Na	0.000	0.000	0.000	0.000	0.000	0.000	0.000	0.000
K	0.000	0.000	0.000	0.000	0.000	0.000	0.000	0.000
P	0.000	0.000	0.000	0.000	0.000	0.000	0.000	0.000
Total	2.970	3.000	2.000	2.000	3.000	3.000	1.000	1.000

Fe^{3+} recalculated on the basis of stoichiometry.
Zero stands for 'too low' values of oxides, measured by EPMA, whereas NA values are not measured.

versus A/CNK bivariate plot (Fig. 6d; Shand, 1943). The studied rock is mildly miaskitic with an agpaitic index (molar Na + K/ Al) varying in the range of 0.83–0.94 (Fig. 6e).

The studied rock is characterized by low concentrations of compatible elements, namely Ni (up to 4 ppm, 10 ppm in one sample (NP102C)), Cr (up to 20 ppm) and Co (up to 60 ppm) and shows highly variable concentrations of the LILEs (e.g. Rb (~41–164 ppm), Sr (~129–1963 ppm) and Ba (~177–6551 ppm)) and moderate to high concentrations of high field strength elements (HFSEs) (e.g. Zr (~5–601 ppm), Hf (~0–13 ppm), Nb (~40–159 ppm) and Ta (~2–9 ppm)). On the multi-element spidergram, normalized against the primitive mantle (after McDonough & Sun, 1995), the studied rock shows enriched LILEs and HFSEs (Fig. 7a; enrichment of Ti = 3–5 times, Nb and Ta = 80–110 times, Zr and Hf = 15–60 times, barring three samples with <10 times enrichment). Enriched concentrations of LILEs and HFSEs are characteristics of alkaline rocks around the world (Woolley *et al.* 1995; Eby *et al.* 1998; Upadhyay & Raith, 2006; Upadhyay *et al.* 2006*a*,*b*,*c*). The primitive-mantle normalized multi-element

spidergram shows a prominent positive anomaly for Ba, negative anomaly for Ti, Zr, Hf, Th and U, and mildly negative anomaly for Pb in the bulk of the samples. Mean values for the Nb/Ta and Zr/Hf ratios of the samples are close to chondritic values of 17 ± 5 and 42 ± 10, respectively, but with greater scatter (Nb/Ta = 19.9 and Zr/Hf = 34.4; reviewed in Huang *et al.* 2011; Pfander *et al.* 2012). However, one sample (NP62) has an extremely high Zr/ Hf ratio (~3900), which could be related to the anomalously low Hf content (0.055 ppm) in the sample. The geochemical features of Pb and Ti and the Nb/Ta, Zr/Hf and Th/U (3.6 ± 2) ratios are consistent with a dominant input from a mantle source relative to the continental crust (Upadhyay *et al.* 2006*b*). The average Nb/U ratio (>300) and Ce/Pb ratio (>30) of the samples are much higher as compared to the supra-subduction zone continental crust (Nb/ U = 47 ± 10 and Ce/Pb = 25 ± 5; Hofmann *et al.* 1986) and also point towards a mantle source. In the chondrite-normalized REE diagram (after McDonough & Sun, 1995), the studied rock shows strongly fractionated and enriched light rare earth elements (LREE; $(La/Lu)_N$ ~23–87) and a weakly sloping to nearly flat heavy
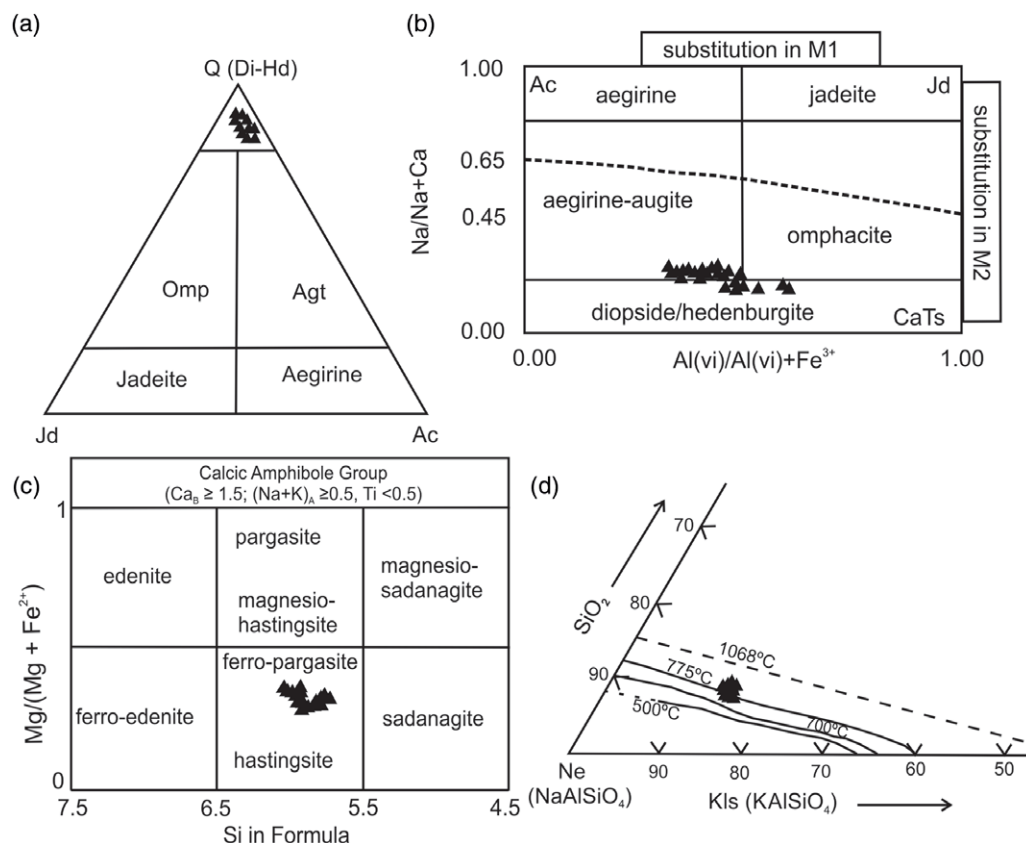
Fig. 5. (a) Clinopyroxene compositions plotted on the Q (quadrilateral pyroxene) – jadeite (Jd) – aegirine (Ac) diagram (Morimoto, 1988). (b) Clinopyroxene compositions extend across the boundaries between diopside–hedenbergite and aegirine–augite on the Na/(Na + Ca) versus $Al_{VI}/(Al_{VI} + Fe^{3+})$ atoms per formula unit diagram. (c) Amphibole compositions plot in the field of hastingsite to ferro-pargasite on the Mg number versus Si (apfu) diagram for calcic amphiboles by Leake *et al.* (1997). (d) Nepheline compositions plotted on the normative nepheline (Ne) – kalsilite (Kls) – silica (Qtz) triangular diagram (Tilley, 1954).

rare earth elements (HREE) pattern (Fig. 7b). In contrast to many reported alkaline rocks (Woolley *et al.* 1995; Eby *et al.* 1998; Upadhyay *et al.* 2006*b*; Upadhyay & Raith, 2006), the chondrite-normalized REE pattern of the studied rock shows a distinct positive Eu anomaly that is mirrored by high Sr concentrations (Fig. 7b; Upadhyay *et al.* 2006*c*). A positive correlation between Eu and Sr is noted (Fig. 8). This can be explained by replacement of Ca in the mineral structure (e.g. plagioclase, clinopyroxene and apatite) by Sr and Eu^{2+} at low fO_2 conditions (discussed in Section 7.b).

The Mg no. (molar $MgO/MgO + FeO_t$) of the studied rock varies within a reasonably large spread from ~3 to 30. This raises the possibility that the magmatic protolith of the studied rock could undergo fractional crystallization (reviewed in Rollinson, 1993). In view of the compositional variation of some metamorphic minerals (e.g. amphibole, biotite) in millimetre size domains (or even less), element mobility during the superposed metamorphism is unlikely to alter the bulk compositions of the large sample used for bulk compositions. Studies have shown that the observed bulk-rock compositions are the end product of various processes including variation of source rock composition, degree of partial melting of the source rock, assimilation and fractional crystallization (reviewed in Philpotts & Ague, 2009). Notwithstanding these problems, the compositional variations of the different major and trace elements (including REEs) are shown against the variation in Mg no. (used as a differentiation index; Figs 9, 10). Considering the uncertainties associated with the bivariate plots of rocks, Figure 9 shows a positive correlation of SiO_2, TiO_2, FeO, CaO and P_2O_5 and negative correlation of Na_2O, whereas Al_2O_3 and K_2O show a scattered plot with respect to Mg no. Such trends are common during magmatic fractionation. There is a strong positive correlation (R^2 value = 0.92)

between K_2O and Al_2O_3 (Fig. 8). These compositional features that can be attributed to modal variation of K-feldspar in the studied rock due to the presence of K-feldspar cumulates in many samples (Fig. 4c). A large scattering of data on the Rb + Ba versus K_2O plot suggests exchange of Rb and Ba between K-feldspar (dominant reservoir of Ba and Rb) and biotite (reservoir of Rb) with local metamorphic fluid (Fig. 8; Imeokparia, 1981). A similar process has been documented from the millimetre to centimetre sized charnockitic veins in the amphibolite-facies rocks (the 'incipient charnockitization'; Newton, 1992; Touret *et al.* 2019). CaO and P_2O_5 also show a strong positive correlation (Fig. 8; R^2 ~0.97). Barring one data point (NP94B that has the highest (La + Ce) = 235 ppm and CaO = 9.45), a distinct positive correlation between CaO and (La + Ce) is noted (R^2 ~0.63). Inclusion of this odd data point reduces the R^2 value to ~0.47 (Fig. 8). Together with the positive correlation of CaO, P_2O_5, La and Ce with Mg no. (Figs 9, 10), all these compositional features suggest fractionation of apatite, presumably during differentiation of the magmatic protolith. The strong positive correlation between CaO and MgO (R^2 ~0.97) is consistent with fractionation of clinopyroxene, presumably during magmatic differentiation (Fig. 8). Together with the positive correlation of CaO, TiO_2 and FeO with Mg no. (Fig. 9), the positive correlation of FeO and CaO with TiO_2 (Fig. 8) can be best explained by fractionation of ilmenite and titanite during the magmatic processes. A negative Zr anomaly in the primitive-mantle normalized trace-element spidergram suggests that either zircon, the chief reservoir of Zr, also fractionated early or the source itself was poor in Zr (Fig. 7a). The scatter of Ni, Cr and Co with Mg no. (Fig. 10) suggests that the variation of concentrations of these elements is controlled by variable amounts of magnetite (the reservoir of Ni, Co and Cr) present in different samples.

Table 8. Representative bulk composition of Kusumdih nepheline syenite

Sample	NP32A	NP32C	NP42A	NP42B	NP64A	NP66A	NP66B	NP75	NP81	NP82	NP97	NP99	NP102C	NP103	NP62	NP47X	NP91A	NP94B
SiO$_2$ (wt%)	53.88	52.62	56.85	54.66	52.37	52.49	50.97	53.9	52.72	53.59	51.32	52.38	55.27	55.71	53.84	46.98	44.8	43.98
TiO$_2$	0.32	0.44	0.68	0.52	0.38	0.40	0.50	0.36	0.41	0.32	0.51	0.47	0.34	0.35	0.13	1.77	2.36	2.79
Al$_2$O$_3$	22.13	22.01	19.89	21.40	22.17	22.31	22.27	21.62	21.78	23.08	21.94	23.05	22.06	22.08	20.29	18.87	16.20	17.50
FeO$_t$	5.75	5.42	6.39	5.94	5.30	5.38	6.44	5.69	6.63	5.34	6.58	5.51	4.58	5.16	5.27	12.44	15.80	13.51
MnO	0.07	0.08	0.10	0.09	0.07	0.06	0.08	0.07	0.08	0.06	0.10	0.07	0.06	0.06	0.09	0.20	0.25	0.18
MgO	0.29	0.62	0.53	0.53	0.42	0.45	0.48	0.37	0.47	0.75	0.55	0.60	0.57	0.28	0.1	1.84	2.79	3.19
CaO	2.20	3.00	2.54	2.04	1.84	1.72	2.24	2.00	1.99	1.69	2.40	2.02	2.08	1.11	1.26	6.33	8.01	9.45
Na$_2$O	4.93	5.39	6.34	7.77	6.56	6.51	5.79	6.67	6.71	5.86	6.13	6.20	5.36	6.69	6.57	2.80	1.99	1.42
K$_2$O	8.09	8.19	6.35	6.79	7.84	7.97	7.87	7.34	7.54	7.96	8.00	8.76	7.94	7.14	6.73	5.89	4.58	5.19
P$_2$O$_5$	0.14	0.18	0.25	0.22	0.18	0.17	0.20	0.16	0.22	0.15	0.24	0.22	0.09	0.11	0.03	0.71	1.16	1.27
Rb (ppm)	108.80	102.85	125.58	142.19	142.28	139.81	109.91	128.77	147.51	112.87	130.67	114.40	103.37	105.93	164.27	76.79	56.48	40.65
Sr	1041.46	933.91	1236.17	1077.97	553.83	552.97	1140.47	555.13	471.15	533.79	1143.54	806.01	566.65	330.62	128.94	590.09	1736.16	1962.77
Ba	2208.09	2089.37	6551.04	5108.16	2904.59	3031.54	4273.05	2633.01	2236.53	2340.20	5194.33	5235.07	1909.06	897.30	177.25	695.98	2314.99	1711.56
Zr	136.45	69.69	294.79	365.67	251.90	276.68	429.36	214.77	414.03	4.67	402.44	563.72	314.77	25.31	216.39	309.79	601.23	198.65
Nb	56.06	39.55	84.20	72.08	72.30	106.78	78.57	42.23	98.36	50.66	61.15	103.39	70.59	42.76	87.44	84.39	159.09	38.89
Hf	6.74	4.17	6.39	7.36	6.52	6.72	9.63	5.95	9.26	0.08	8.29	10.84	7.79	0.62	0.06	6.48	12.79	4.33
Ta	5.24	6.07	5.98	3.68	4.36	4.35	4.21	2.21	4.17	2.09	4.19	5.54	3.66	2.54	8.44	8.76	7.78	2.28
Pb	6.22	8.59	5.93	4.16	3.46	3.14	3.63	2.85	3.43	4.08	4.77	4.68	3.96	2.66	15.74	7.63	6.49	3.11
Y	9.50	7.03	18.67	16.46	15.34	13.24	17.82	11.88	16.60	12.25	18.04	23.39	11.65	7.91	8.94	26.98	61.35	36.71
Co	7.88	4.25	74.04	43.20	33.72	42.00	36.07	50.01	44.88	29.97	43.43	34.88	43.56	40.85	60.58	14.28	47.05	45.65
Ga	22.68	23.62	27.43	28.04	26.52	26.11	28.37	25.58	27.37	25.82	28.43	26.91	27.84	24.62	27.57	27.45	33.74	26.79
Cr	4.04	1.42	1.58	0.44	1.92	0.69	1.11	0.64	1.06	2.53	0.81	0.78	12.12	0.66	0.03	20.04	1.67	1.79
V	2.00	0.59	1.99	1.50	0.10	0.28	1.26	0.49	1.87	1.51	1.28	1.60	8.89	1.02	1.25	3.55	9.05	27.49
Ni	2.19	0.00	3.20	2.25	4.02	1.13	3.08	0.86	1.81	1.63	3.39	0.86	9.90	0.84	0.36	2.76	4.64	7.76
La	40.29	35.98	58.24	51.04	49.20	46.11	62.34	53.12	56.47	73.95	60.05	65.59	33.47	40.20	32.26	86.32	142.72	72.34
Ce	67.53	60.60	120.38	108.23	101.36	106.30	132.21	109.25	129.51	150.71	126.65	140.25	81.73	86.70	48.52	136.25	323.78	162.94
Pr	9.57	8.62	14.58	12.54	13.10	13.96	14.84	11.71	14.83	15.57	13.84	16.20	9.42	9.15	6.70	19.56	34.07	20.06
Nd	32.38	29.55	56.29	47.56	50.49	54.58	55.38	44.95	59.15	56.70	52.49	60.96	36.44	34.27	22.28	59.68	134.91	88.14
Sm	6.39	5.63	10.54	9.37	9.16	10.07	10.63	8.93	11.70	10.30	10.33	11.70	7.58	6.40	4.10	12.00	30.80	18.74
Eu	2.81	2.36	12.05	8.04	6.60	6.44	8.08	5.40	4.82	4.93	7.85	8.18	4.06	4.14	1.10	3.32	12.31	10.07
Gd	5.94	5.41	10.29	8.45	9.23	9.54	10.05	7.79	10.26	9.40	9.99	11.42	6.50	5.74	4.06	11.69	26.58	17.76
Tb	0.73	0.62	1.26	1.10	1.06	1.08	1.26	0.96	1.31	1.08	1.21	1.43	0.88	0.67	0.54	1.45	3.81	2.29

(Continued)

Table 8. (*Continued*)

Dy	3.12	2.62	5.25	4.59	4.33	4.28	5.15	3.69	5.17	3.91	5.04	6.18	3.62	2.57	2.63	6.79	16.42	9.81
Ho	0.40	0.34	0.81	0.70	0.64	0.60	0.77	0.52	0.75	0.56	0.75	0.97	0.53	0.35	0.37	0.97	2.70	1.60
Er	0.98	0.80	1.99	1.74	1.55	1.37	1.92	1.27	1.81	1.37	1.89	2.43	1.33	0.85	0.92	2.47	6.92	3.99
Yb	0.58	0.46	1.13	0.96	0.83	0.68	1.12	0.64	0.96	0.68	1.02	1.34	0.80	0.39	0.59	1.71	4.33	2.33
Lu	0.09	0.08	0.15	0.12	0.10	0.09	0.16	0.08	0.13	0.09	0.13	0.16	0.11	0.05	0.09	0.29	0.58	0.32
Th	0.67	1.40	1.02	1.46	1.05	0.21	0.44	0.19	1.10	0.27	1.41	4.24	1.00	0.10	0.88	0.00	7.02	1.95
U	0.81	0.44	0.27	0.32	0.42	0.05	0.08	0.03	0.25	0.06	0.33	1.50	0.50	0.01	0.50	0.01	1.99	0.62
Mg#	8.24	16.93	12.88	13.71	12.38	12.98	11.72	10.39	11.21	20.01	12.97	16.25	18.17	8.83	3.27	20.86	23.94	29.62
Na$_2$O+K$_2$O	13.02	13.58	12.69	14.56	14.40	14.48	13.66	14.01	14.25	13.82	14.13	14.96	13.30	13.83	13.30	8.69	6.57	6.61
K$_2$O/Na$_2$O	1.64	1.52	1.00	0.87	1.20	1.22	1.36	1.10	1.12	1.36	1.31	1.41	1.48	1.07	1.02	2.10	2.30	3.65
Nb/Ta	10.70	6.52	14.09	19.57	16.60	24.53	18.68	19.11	23.57	24.30	14.61	18.65	19.29	16.86	10.36	9.64	20.45	17.04
Zr/Hf	20.25	16.72	46.13	49.70	38.62	41.20	44.60	36.07	44.70	58.71	48.56	51.99	40.42	40.64	3886.44	47.78	46.99	45.92
Th/U	0.83	3.19	3.77	4.61	2.50	3.97	5.64	6.90	4.44	4.34	4.28	2.83	2.02	7.21	1.75	0.29	3.54	3.16
Rb+Ba	2316.89	2192.22	6676.62	5250.35	3046.87	3171.36	4382.96	2761.78	2384.04	2453.08	5325.00	5349.47	2012.43	1003.23	341.52	772.78	2371.47	1752.21
La+Ce	107.82	96.58	178.62	159.27	150.56	152.41	194.56	162.37	185.98	224.66	186.71	205.84	115.20	126.90	80.78	222.57	466.51	235.27
Nb/U	69.50	89.83	311.02	227.49	172.13	1982.12	997.90	1566.18	396.48	799.89	186.07	68.95	142.53	3025.44	173.90	5761.11	80.07	62.97
Ce/Pb	10.85	7.06	20.31	25.99	29.27	33.82	36.42	38.30	37.78	36.94	26.54	29.99	20.64	32.64	3.08	17.86	49.91	52.45
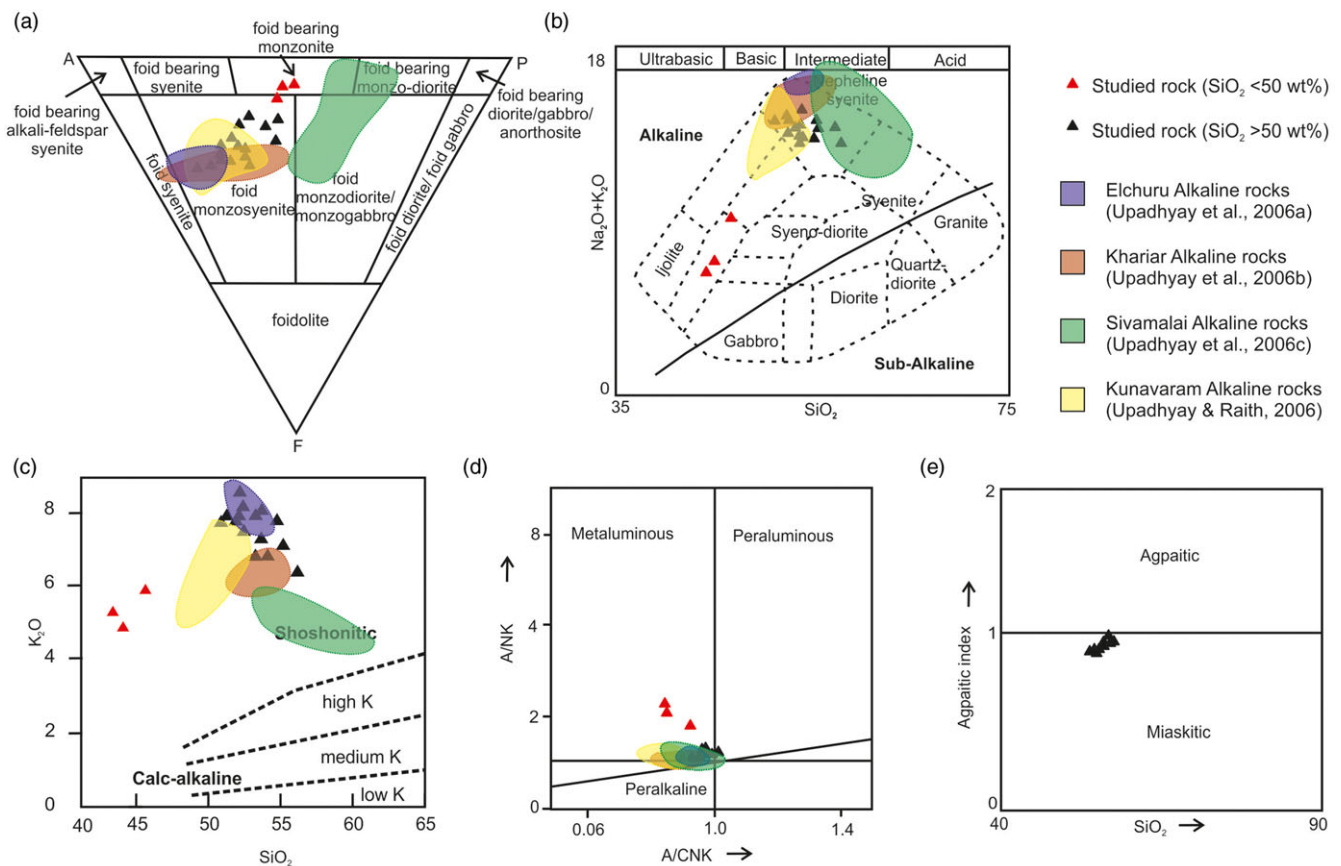
Fig. 6. (Colour online) (a) The studied rock falls in the 'foid-monzosyenite' and 'foid-bearing monzonite' field on the Feldspathoid – Plagioclase feldspar – Alkali feldspar (FAP) diagram (Le Maitre, 2002). (b) The Total Alkali Silica (TAS) diagram suggests that most of the samples are of 'nepheline syenite'; with some plotting in between the fields of ijolite and gabbro (Le Bas *et al.* 1992). (c) The samples plot in the 'shoshonite' field on the K_2O versus silica diagram (Peccerillo & Taylor, 1976). (d) The molar A/NK versus A/CNK diagram reveals that the rock samples are 'metaluminous' to 'peralkaline' in nature (Shand, 1943). (e) Samples appear to be slightly miaskitic when plotted on the Agpaitic index (molar Na + K/Al) versus SiO_2 plot. Fields for bulk-rock data from other DARs from India (Upadhyay & Raith, 2006; Upadhyay *et al.* 2006*a,b,c*) have been included in diagrams (a–d).

Fractionation of clinopyroxene and the accessory phases, e.g. apatite, ilmenite and titanite, during differentiation presumably enriched the residual liquid with SiO_2, which is reflected in the positive correlation of Mg no. and SiO_2 (Fig. 9). Apatite, ilmenite and titanite are the source of LREEs and HFSEs. Fractionation of these minerals are, therefore, likely to deplete the rocks with these elements. However, like most of the alkaline rocks of the world, the studied rock also shows enrichment of LREEs and HFSEs (Fig. 7a). There exist two possibilities to explain these particular features. These are:

(1) After fractionation of apatite, ilmenite and titanite, the residual melt was still sufficiently enriched in FeO, TiO_2, CaO and P_2O_5 to crystallize these phases. Fractionation of titanite and apatite during early fractionation of alkaline magma has been reported from many places (e.g. Upadhyay *et al.* 2006*c*).

(2) The positive correlations of FeO, TiO_2, CaO and P_2O_5 with Mg no. (Fig. 9) are accidental and the variation of $CaO–P_2O_5$, $TiO_2–FeO$ and $CaO–TiO_2$ (Fig. 8) is controlled by the variation of the abundance of apatite and titanite in different samples.

Though it is difficult to discriminate between the two possibilities, a combination of the two processes seems likely.

7. Discussion

7.a. Formation of the magmatic protolith

Field and petrographic features demonstrate that the studied nepheline syenite is deformed and metamorphosed; hence it can be categorized as a DAR (Burke *et al.* 2003; Burke & Khan, 2006; Leelanandam *et al.* 2006). Tracing the magmatic characters of a suite of deformed and metamorphosed nepheline syenite on the basis of the geochemistry presupposes that the studied rock virtually retains its magmatic chemistry at least at the scale of the sample used for chemical analyses. Studies have shown that unless the rocks are extensively metasomatized or suffer significant melt loss at very high temperatures, mobility of many elements is restricted within a few millimetres (e.g. Chowdhury *et al.* 2013). The studied rock is not extensively metasomatized; neither is there any evidence of significant melt loss during metamorphism. Grain-scale metasomatism was certainly operative to form metamorphic hydrous minerals. Furthermore, the geochemical data do not support significant crustal contamination at any stage of evolution of the rocks. We therefore presume that the composition of the magmatic protolith of the studied rock did not change significantly at the scale of the hand specimen. Our study, thus, corroborates the view of published work that the magmatic characters are retained in the studied rock (Upadhyay & Raith, 2006; Upadhyay *et al.* 2006*b,c*; Burke *et al.* 2008; Ashwal *et al.* 2016; Paul *et al.* 2020).

7.a.1. Geochemical proxy of the studied rock: source characteristics versus crustal contamination

A number of geochemical features, namely, (1) enriched Nb and Ta concentrations, (2) Nb/Ta (17 ± 5) and Zr/Hf (42 ± 10) ratios showing near chondritic values, (3) troughs for U, Th, Pb and
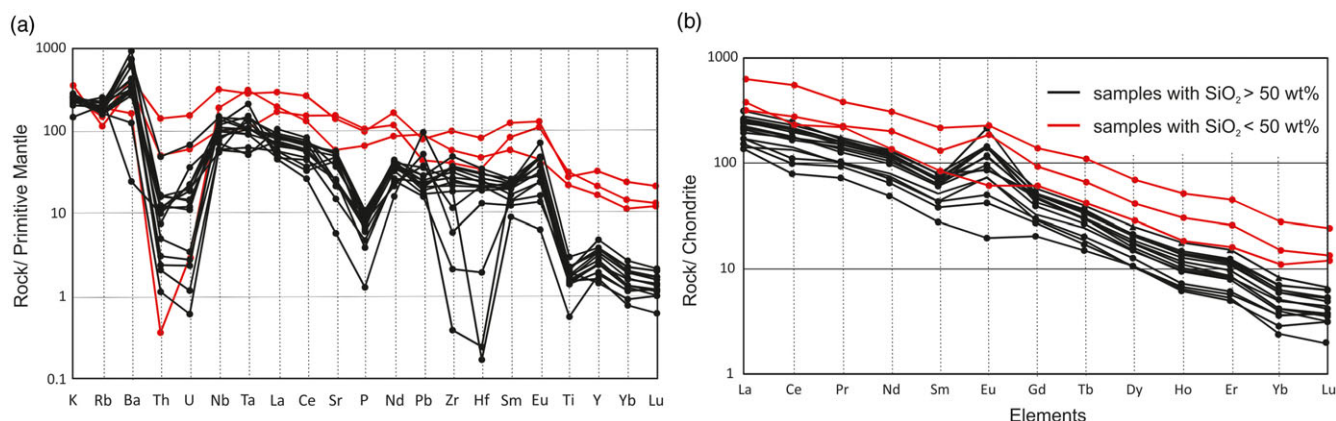
Fig. 7. (Colour online) (a) Primitive-mantle normalized trace-element spidergram (after McDonough & Sun, 1995) and (b) chondrite-normalized rare earth element diagram (after McDonough & Sun, 1995) for the studied rock.
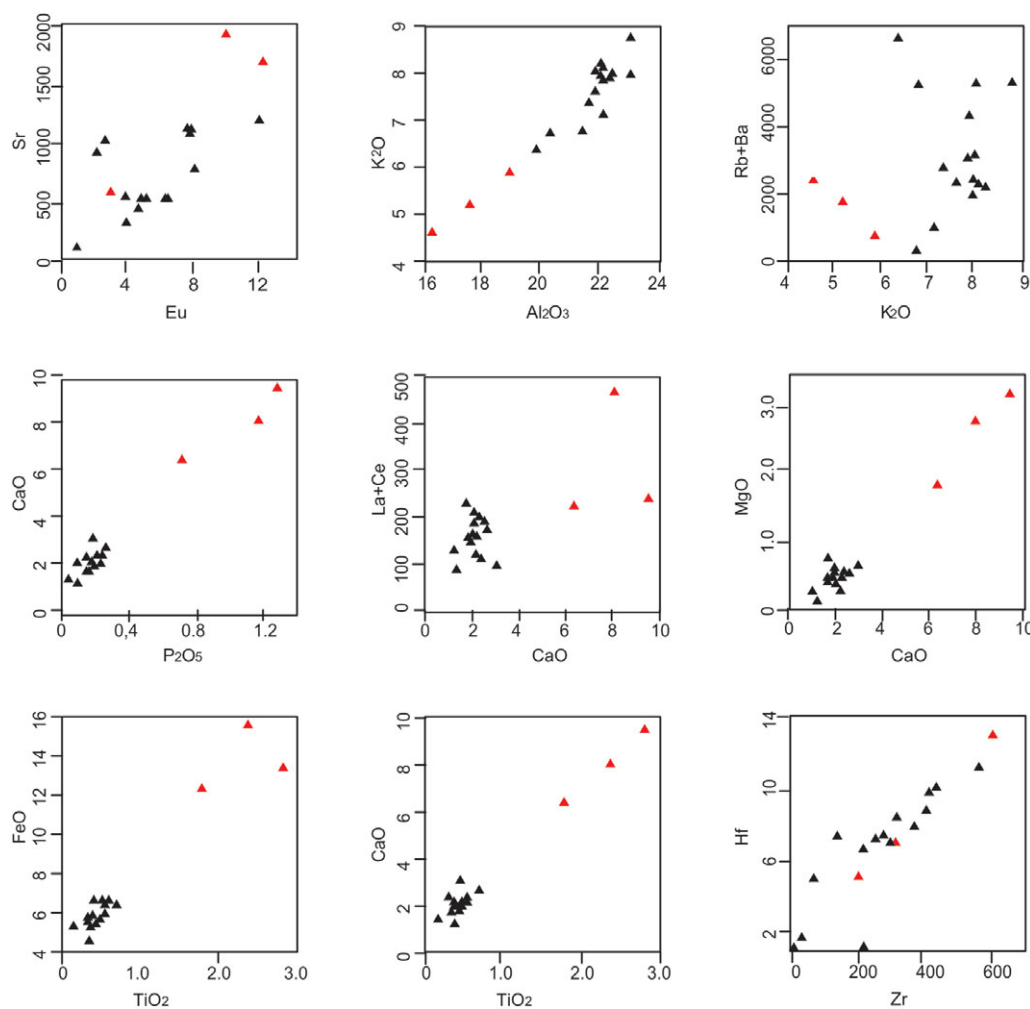

Fig. 8. (Colour online) Selected bivariate diagrams and plots showing the trends in major- and trace-element concentrations. Symbols used for the samples are the same as in Figure 6.

Ti on the primitive-mantle normalized multi-element diagram (Fig. 7a) and (4) high values of Nb/U (>300) and Ce/Pb (>30) are consistent with the view that the magmatic protolith of the studied rock was derived from the mantle with insignificant crustal contamination (Upadhyay *et al.* 2006*b*). In addition to these, the highly fractionated REEs ((La/Lu)$_N$ = 23–87) and the nearly flat

HREEs on the chondrite-normalized diagram (Fig. 7b) suggest that the parental magma of the studied rock was sourced from garnet peridotite in the SCLM (Lucassen *et al.* 2007; Aulbach *et al.* 2008; Pfander *et al.* 2012; Pagano *et al.* 2016; Ashwal *et al.* 2016). Correlation among the major oxides and trace elements suggests variable fractionation of apatite, titanite, ilmenite and
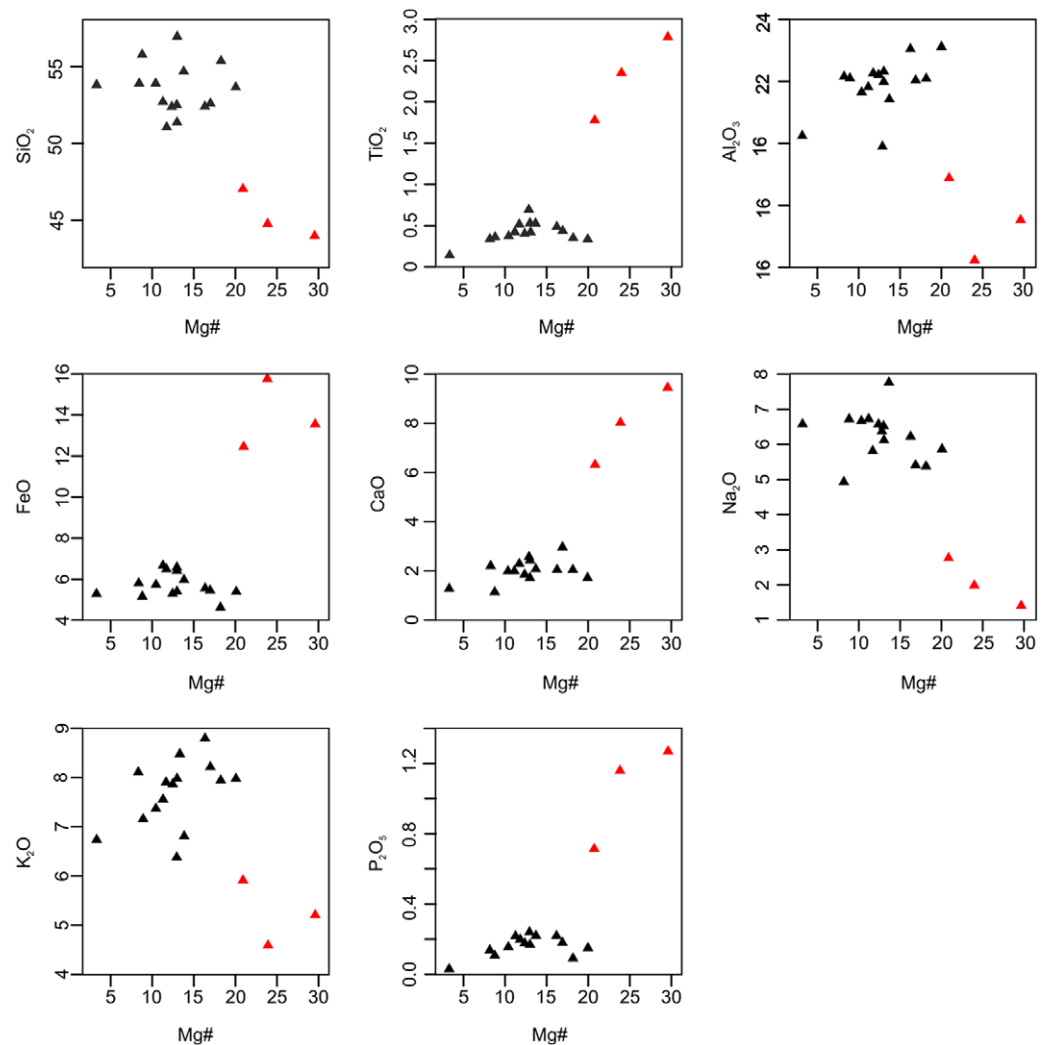
Fig. 9. (Colour online) Variation diagrams of major oxides with concentration of Mg no. (Differentiation Index) showing positive variation trends for SiO$_2$, TiO$_2$, FeO, CaO and P$_2$O$_5$, a negative trend for Na$_2$O and scatter for K$_2$O and Al$_2$O$_3$. Symbols used for the samples are the same as in Figure 6.

clinopyroxene from the parental melt of the studied rock (Figs 8, 9, 10; Morbidelli *et al.* 2000; Zappettini *et al.* 2013). Published information has demonstrated that nepheline syenite magma can be generated from a basanitic melt through fractionation of nepheline and clinopyroxene in the garnet peridotite field of the SCLM, before being emplaced at crustal conditions (Edgar, 1987; Kyle *et al.* 1992; Ablay *et al.* 1998; Eby *et al.* 1998; Upadhyay & Raith, 2006; Irving & Green, 2008; Zappettini *et al.* 2013; Pagano *et al.* 2016). Spatially close associations of basanite and nepheline syenite have been noted in many well-studied alkaline complexes (Eby *et al.* 1998; Pfander *et al.* 2012; Ashwal *et al.* 2016). The presence of a distinct positive Eu anomaly and coupled behaviour of Eu and Sr vouch for low fO$_2$ conditions during magmatic crystallization (Fig. 7b). Lack of evidence for plagioclase fractionation from the early melt is consistent with the fact that the parental melt of the magmatic protolith of the studied rock is likely to be basanitic rather than alkali basalt (Upadhyay & Raith, 2006). In Figure 11, trace and REE patterns of the studied nepheline syenite have been compared with the trace (primitive-mantle normalized) and REE (chondrite-normalized) patterns of a number of well-studied DARs in India and elsewhere in the world (Eby *et al.* 1998; Upadhyay *et al.* 2006*b*,*c*; Upadhyay & Raith, 2006; Casquet *et al.* 2008; Nude *et al.* 2009; Obeid & Lalonde, 2013; Viana & Battilani, 2014; Cheng *et al.* 2018). Despite the fact that (a) these

rocks have different ages and underwent various degrees of fractionation of diverse minerals and assimilation, and (b) there is compositional variation of the SCLM from which the magmatic protoliths of these DARs were sourced, several features that are common between them are noted. These include (a) enriched concentrations of LILEs and HFSEs, (b) peaks for Eu (except the Malawi occurrence) and troughs for U and Th, and (c) highly fractionated chondrite-normalized REE patterns with enriched LREEs and nearly flat HREEs. The trace and REE patterns of the studied rock matches the best with the trace and REE patterns of the nepheline syenite reported from the Indian occurrence at Elchuru, from the Eastern Ghats Mobile Belt (EGMB), and Kpong from Ghana, West Africa (Fig. 11). In all these localities (shown in Fig. 11), the alkaline magmas are considered to be sourced from the low-degree partial melting of metasomatized SCLM in the field of garnet peridotite (see the references in Fig. 11). The low degree of partial melting of deep and enriched SCLM was achieved by adiabatic decompression melting due to extension of the lithosphere including the continental crust (McKenzie, 1989; Ghiorso *et al.* 2002; Smith & Asimow, 2005). Extension of the continental lithosphere is common under a continental rift that may or may not lead to the opening up of an ocean basin (reviewed in Ashwal *et al.* 2016; Das *et al.* 2019). This observation may explain the restricted occurrence of alkaline rocks and carbonatites (and their metamorphosed
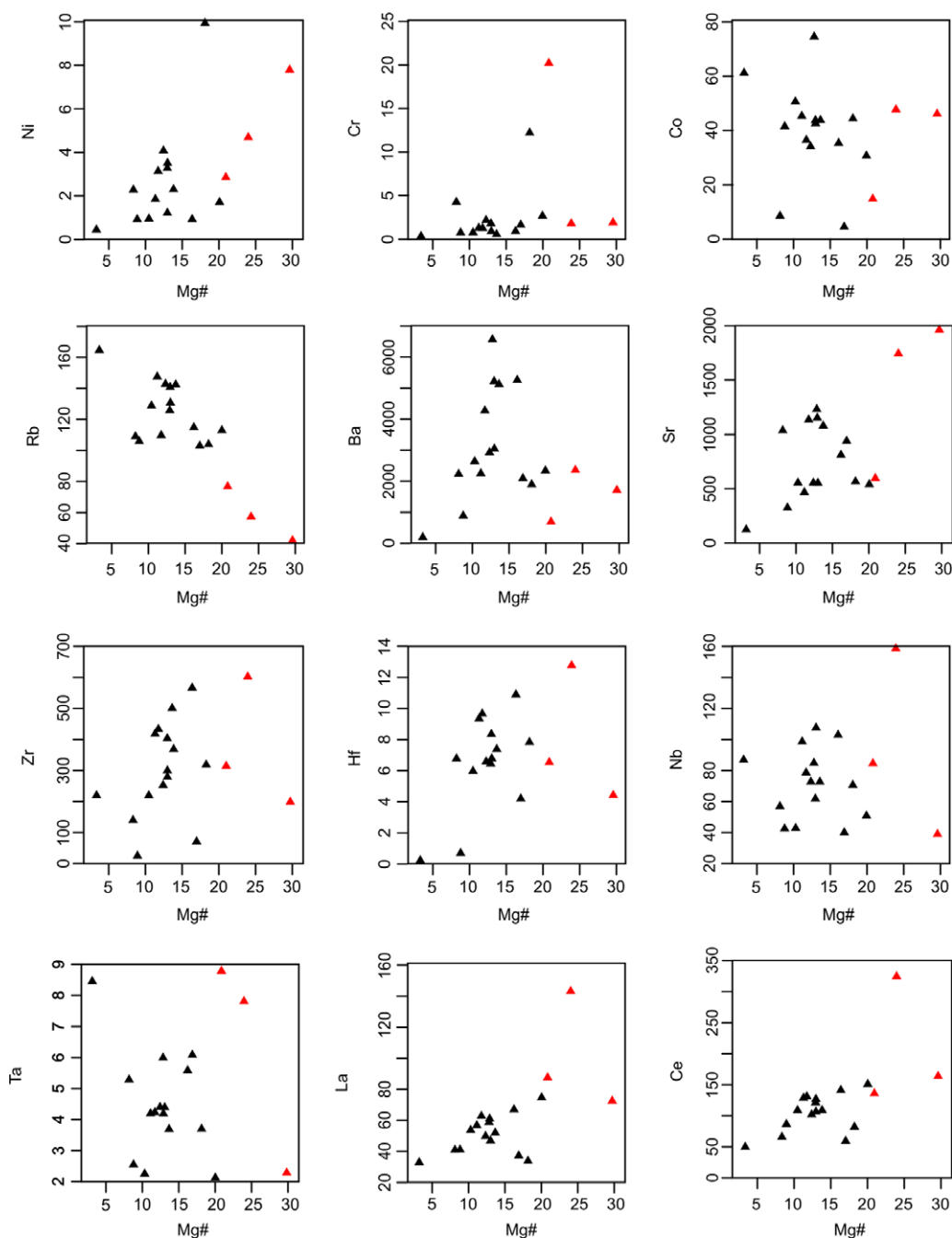
Fig. 10. (Colour online) Trace-element variation diagrams with concentration of Mg no. (Differentiation Index). Symbols used for the samples are the same as in Figure 6.

equivalents) in extant and extinct continental rift zones (Eby *et al.* 1998; Upadhyay, 2008; Ashwal *et al.* 2016; Paul *et al.* 2020). It, therefore, stands to reason that the NPSZ and its DARCs represent an extinct continental rift. On the basis of geochemistry and Pb, Nd, Hf and Sr radioisotopic compositions, different types of mantle reservoirs (high-μ (HIMU), enriched mantle (EM), focal zone (FOZO), deleted mantle (DM), depleted mid-ocean ridge mantle (DMM)) are recognized (reviewed in Castillo, 2016). Depleted mantle is considered to be the dominant component in the SCLM (Ashwal *et al.* 2016).

There exists a considerable debate regarding the LILE- and HFSE-rich mantle source for the alkaline rocks and carbonatite (ARCs). The chief views are as follows:

A. Contribution of the sub-lithospheric (asthenospheric) mantle source in the SCLM. Through their detailed study including field relationships, textural observations and exhaustive analyses of geochemistry (including Nd and Pb isotopic data), Prelevic *et al.* (2004) demonstrated that mixing of a felsic (dacitic) and lamproitic magma can generate LILE-, HFSE- and LREE-enriched melts. Subcontinental sources (mixing of two or more components from HIMU, EM, FOZO, DM, DMM) for the ARC magmas are also supported by Bell & Tilton (2001), Bizimis *et al.* (2003) and Bell & Simonetti (2010).

B. Lithospheric mantle source with insignificant contribution from asthenospheric mantle. Early studies on Precambrian ARCs of the Canadian Shield suggested that these rocks had a DM source
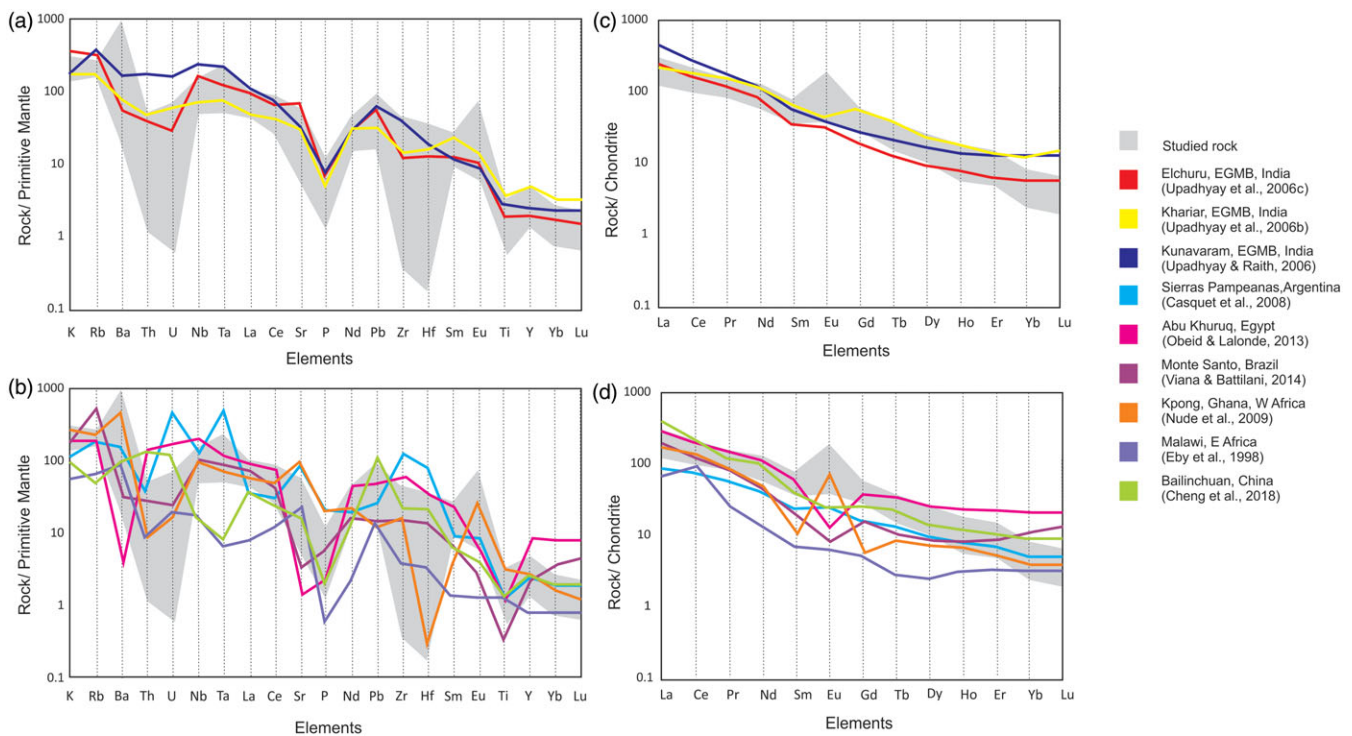
Fig. 11. (Colour online) Primitive-mantle normalized trace-element spidergram for the studied rock compared with (a) the nepheline syenite occurrences in India, and (b) the nepheline syenite occurrences from across the world. Chondrite-normalized rare earth element diagram for the studied rock compared with (c) the nepheline syenite occurrences in India, and (d) the nepheline syenite occurrences from across the world. Average values are plotted for other occurrences, whereas a zone has been marked for the studied rock (Eby *et al.* 1998; Upadhyay & Raith, 2006; Upadhyay *et al.* 2006a,b,c; Casquet *et al.* 2008; Nude *et al.* 2009; Obeid & Lalonde, 2013; Viana & Battilani, 2014; Cheng *et al.* 2018).

(Bell & Blenkinsop, 1987). However, enriched concentrations of HFSEs, Nd and Sr (>50 times relative to DM) in many ARCs and DARCs require one or more additional components that could provide these elements (reviewed in Ashwal *et al.* 2016). With detailed geochemical and isotopic studies on the deformed and undeformed ARCs from Southern Africa, Ashwal *et al.* (2016) demonstrated that mixing of a small amount of older DARs (<2 %) with DM can explain the geochemical characters of the undeformed younger alkaline rocks. The ARC–DAR link has been demonstrated from different localities of the world including occurrences in Russia, Africa, India and the Grenville Province of the USA (Burke *et al.* 2003, 2008; Burke & Khan, 2006; Leelanandam *et al.* 2006).

Das *et al.* (2019) suggested that the nepheline syenite in the studied area was emplaced between 950 and 900 Ma. A number of studies have demonstrated that a magmatic arc was formed in the basement of the CGGC (~2200 Ma model age) between 1720 and 1670 Ma (Mukherjee *et al.* 2019a,b). Records of magmatism and metamorphism of similar (or older) ages have been recorded from the fold belts that presumably stitched together the Archaean cratons of peninsular India during the formation of the Columbia supercontinent (Rogers & Santosh, 2002; Zhang *et al.* 2012; Sarkar & Schenk, 2016; Sharma *et al.* 2019; Olierook *et al.* 2019). The Palaeoproterozoic Indian shield subsequently broke up and reassembled in the subsequent supercontinent cycles (Rodinia and Gondwana; reviewed in Meert & Torsvik, 2003; Brown, 2007; Li *et al.* 2008; Bhowmik *et al.* 2012; Sengupta *et al.* 2015; Dasgupta *et al.* 2013a; Chattopadhyay *et al.* 2015; Olierook *et al.* 2019). The Indian shield including the CGGC has been punctured by multiple phases of alkaline magmatism with or without carbonatite (reviewed in Paul *et al.* 2020)

and kimberlite/lamproite/lamprophyre (reviewed in Chalapathi Rao *et al.* 2004, 2012, 2020; Rao *et al.* 2016; Sharma *et al.* 2019) that spread over a long stretch of time after the formation of the Indian shield as a part of the Columbia supercontinent. Geochemical and radiogenic isotope data from >1000 Ma kimberlite/lamproite/lamprophyre and the entrained perovskite support the existence of a metasomatized SCLM where DM was the chief component with variable contributions from the asthenospheric mantle (Rao *et al.* 2016; Sharma *et al.* 2019).

The Palaeoproterozoic basement of the CGGC underwent rifting that outpoured huge felsic magmas at ~1450 Ma (reviewed in Mukherjee *et al.* 2018a). During ~1000–950 Ma, these voluminous felsic magmas and the Palaeoproterozoic basement were buried to deep crustal levels, in a continent–continent collisional setting (~10–13 kbar; Mukherjee *et al.* 2017; Dey *et al.* 2019b,c). An association of felsic magma and nepheline syenite has been reported from many rift settings (Eby *et al.* 1998; Ahmed *et al.* 2018). Although no older DARC (>950 Ma) is hitherto reported from the CGGC, the possibility that the Grenvillian (or older) orogenesis in the CGGC transported >950 Ma old DARCs to the deep mantle cannot be ruled out. Transport of DARCs deep into the mantle has been advocated in many studies and is considered as an important source of carbon in the deep mantle (Burke & Khan, 2006; Burke *et al.* 2008; Ashwal *et al.* 2016; Castillo, 2016). In view of the foregoing analysis it is likely that the LILE- and HFSE-rich magmatic protolith of the studied nepheline syenite could originate through a low degree of partial melting of an SCLM containing relics of older DAR/DARC. However, in addition to older DARCs, the SCLM beneath the >950 Ma crust of the CGGC could also have received contributions from other sources (e.g. from fluid derived from the subducted oceanic crust (Castillo, 2016) or a mixture of HIMU and
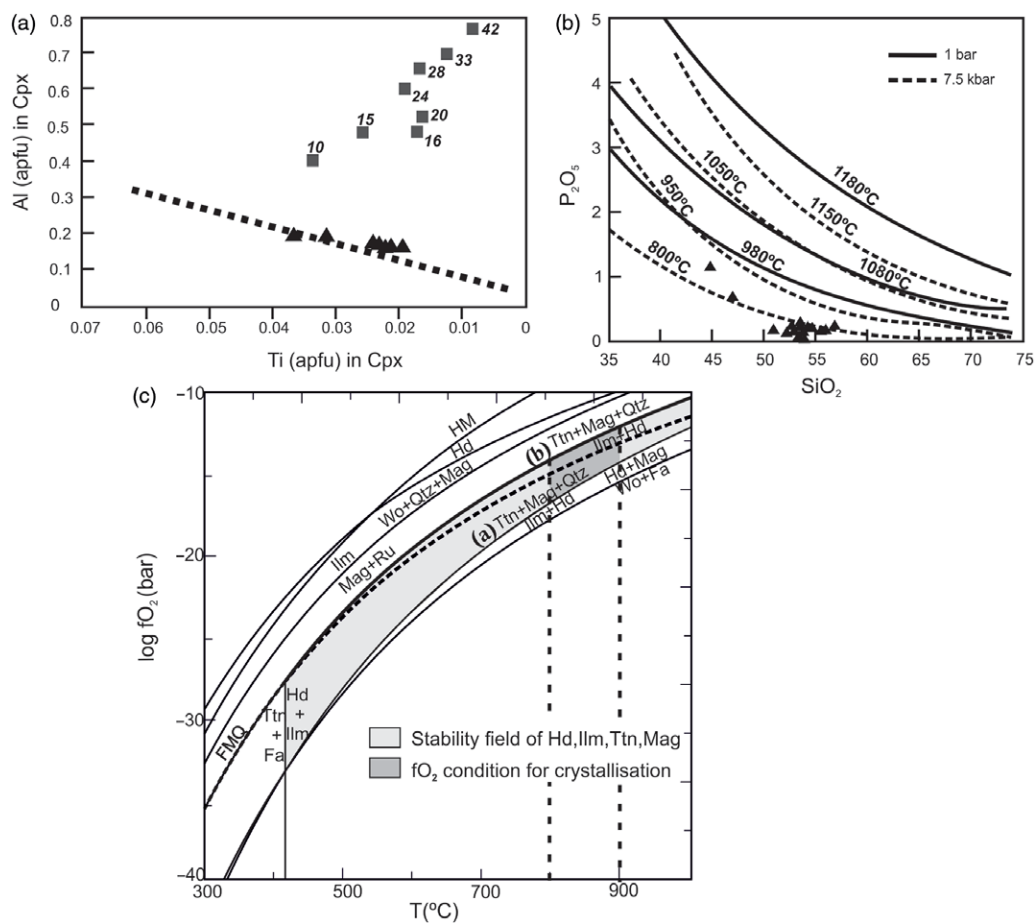
Fig. 12. (a) Al and Ti content of the clinopyroxene, which suggest the crystallizing pressure of the clinopyroxene from the studied rock was below 10 kbar (Thompson, 1974). The squares represent the experimental pressures in terms of Ti and Al content of clinopyroxene. (b) Apatite saturation temperature gives an estimate of the near liquidus temperature for the alkaline magma of 900°C (Green & Watson, 1982). (c) log fO_2 versus temperature diagram in the activity constrained CFTSO system indicates low oxygen fugacity conditions for the crystallization of the alkaline magma, below the FMQ buffer, within the stability field of hedenbergite, ilmenite, titanite and magnetite (Wones, 1989; Lindsley, 1991).

EM1 (Eby *et al.* 1998) or metasomatism of SCLM by carbonate–silicate melt generated at >200 km mantle depth (Dasgupta *et al.* 2013*b*)). More studies on the DARCs of the CGGC may address the relative contributions of the different metasomatizing processes that shaped the compositions of the SCLM beneath the CGGC crust before 950 Ma.

7.b. Physical condition of alkaline magmatism

In the nepheline–kalsilite–silica system (Hamilton, 1961; Tilley, 1954), as mentioned earlier, nephelines of the studied rock with lower normative nepheline and higher silica content is plotted within the temperature range bracketed by 750°C and 950°C (at 1 kbar; Fig. 5d). The approximate pressure of crystallization estimated from the Al and Ti contents of the clinopyroxene from the alkaline magma is below 10 kbar (Fig. 12a; Thompson, 1974). Similar temperatures are also recorded from apatite saturation thermometry where temperatures between 750 and 900°C are recorded (Fig. 12b; Green & Watson, 1982). Despite the fact that some magmatic nepheline and apatite could undergo recrystallization during deformation and metamorphism, temperatures of ~800–900°C can be treated as the magmatic temperature at which the magmatic protolith of the studied nepheline syenite was crystallized. A similar crystallization temperature has been encountered for the Cerro Sarambí alkaline complex of NE Paraguay (Gomes *et al.* 2011).

The fO_2 condition during magmatic crystallization of the protolith of the studied rock was calculated using the stability of the hedenbergite (clinopyroxene) + ilmenite + titanite + magnetite

assemblage on the log fO_2 versus T diagram (Fig. 12c). The estimated magmatic temperatures (800–900°C) and the measured compositions of the minerals were used for this computation. Owing to slow diffusion of Fe and Mg in clinopyroxene structure, the magmatic pyroxenes (of larger grain size) are unlikely to reset during metamorphism (Chakraborty & Ganguly, 1991). The different fO_2 buffers shown in Figure 12c are calibrated in the CaO–FeO–TiO$_2$–SiO$_2$–O$_2$ (CFTSO) system (Wones, 1989; Lindsley, 1991). The clinopyroxene of the studied rock has significant MgO contents in its structure (X_{Mg} up to 0.4). Since ilmenite, magnetite and titanite have minimal non-CFTSO components, the presence of MgO will increase the stability of the assemblage ilmenite + hedenbergite by pushing the reaction ilmenite + hedenbergite + O$_2$ → magnetite + titanite + quartz to higher fO_2 values following the principles of chemical thermodynamics. The end-member reaction and the reaction line corrected for clinopyroxene activity are shown in Figure 12c as reactions (a) and (b), respectively.

At the estimated magmatic temperature of 800–900°C (Fig. 12b), the assemblage ilmenite–hedenbergite–titanite–magnetite in the studied rock constrains low fO_2 conditions that vary within 10^{-12} bars (at 900°C) to 10^{-17} bars (at 800°C) (Fig. 12c; Wones, 1989; Lindsley, 1991). The estimated fO_2 value is low as it falls close to or below the fO_2 values obtained from the FMQ (fayalite–magnetite–quartz) buffer at the same temperature range (shown as a stippled line in Fig. 12c). The low fO_2 at the time of magmatic crystallization was consistent with the observation that Eu in the studied rock was in the Eu^{2+} state and replaced Ca^{2+} in Ca-bearing phases including clinopyroxene. This explains the positive

Eu anomaly shown in Figure 7a. This low oxygen fugacity condition is analogous with the nepheline syenite of the Coldwell complex, Ontario ($f\mathrm{O}_2 = 10^{-14} - 10^{-19}$ bars; Mitchell & Platt, 1982).

7.c. A tectonic model for the evolution of the DAR of the studied area

Collating all the geological information, an attempt has been made to trace the evolution of the studied nepheline syenite. It has been mentioned earlier that three so far reported occurrences of alkaline rocks (including this study) and two occurrences of carbonatite are located along two prominent shear zones, the NPSZ and SPSZ, in the CGGC (Fig. 1; Bhaumik *et al.* 1990; Basu, 1993, 2003; Acharyya *et al.* 2006; Goswami & Bhattacharyya, 2008; Goswami & Basu, 2013; Chakrabarty *et al.* 2016; Das *et al.* 2017, 2019; Paul *et al.* 2020). These alkaline rocks and carbonatite share features that signify that the magmatic protoliths of these rocks were emplaced within the granulite crust of the CGGC (in the NPSZ and part of the SPSZ) and were subsequently deformed and metamorphosed. The present study does not provide any direct constraints on the timing of intrusion of the magmatic protolith and the superimposed deformation and metamorphism. Nevertheless, a large geochronological dataset suggests that the rocks of the CGGC underwent high-temperature granulite-grade metamorphism and developed a strong metamorphic fabric (S_2) during the Grenvillian orogeny (~1000–950 Ma; Chatterjee *et al.* 2008, 2010; Maji *et al.* 2008; Karmakar *et al.* 2011; Rekha *et al.* 2011; Sanyal & Sengupta, 2012; Mukherjee *et al.* 2017, 2019b; Chakraborty *et al.* 2019; Dey *et al.* 2019a,c). Field studies suggest that the magmatic protolith of the studied nepheline syenite cuts across this S_2 fabric of the Grenvillian metamorphites and hence is coeval with the mafic dykes that occurred in different parts of the NPSZ and SPSZ (Reddy *et al.* 2009; Mukherjee *et al.* 2018b; Das *et al.* 2019). The magmatic protolith of the studied nepheline syenite and the mafic dykes underwent deformation (produced the regional S_3 fabric), accompanied by amphibolite-facies metamorphism (occurred at conditions of 690–770°C and ~9–10 kbar) at ~900 Ma (Mukherjee *et al.* 2018b; Das *et al.* 2019). In view of this information, it seems likely that the magmatic protolith of the studied nepheline syenite was emplaced between 950 and 900 Ma. This age bracket is consistent with the U–Pb zircon date of ~922 Ma from the nepheline syenite of the SPSZ (Reddy *et al.* 2009). It is now generally accepted that DARs/DARCs represent a change of tectonic polarity from an extensional to compressional regime when the ARs/ARCs are formed and converted to DARs/DARCs, respectively (Burke *et al.* 2003; Burke & Khan, 2006; Leelanandam *et al.* 2006; Ashwal *et al.* 2007; Upadhyay, 2008).

Figure 13 presents an evolutionary model for the deformed nepheline syenite of the studied area based on the geological information presented in the earlier sections. The evolutionary history begins with the formation of the high-grade rocks and the accompanying S_2 fabric during the 1000–950 Ma continent–continent collisional event (Fig. 13a). The SCLM beneath the CGGC was metasomatized and possibly contained patches of older DARs/DARCs as a consequence of Grenvillian (or older) orogenesis. During ~950–900 Ma, the Grenvillian basement and the SCLM beneath, were extended and rifted presumably due to upwarping of the subcontinental lithosphere (Fig. 13b$_1$). As a consequence, a low degree of partial melting of the garnet peridotite in the SCLM generated basanitic melt (Fig. 13b$_1$) that upon fractionation of clinopyroxene, apatite, ilmenite and titanite produced nepheline syenite magma, which intruded the Grenvillian basement of the CGGC along the NPSZ (Fig. 13b$_2$). No discordance

in terms of continuity of lithology, grade and age of metamorphism were noted across the NPSZ. Neither does the NPSZ expose any high-pressure mafic granulite. It is, therefore, likely that the continental rift in which the magmatic protolith of the studied rock and the adjoining carbonatite were emplaced did not evolve into an open ocean basin. We presume that the NPSZ with its alkaline rocks and carbonatite represents a 'failed' rift, similar to the east African rift zone. A change in tectonic polarity from an extensional to a compressional regime presumably in a continent–continent collisional setting deformed (generation of the regional S_3 fabric) and metamorphosed the high-grade gneissic rocks of the CGGC including the alkaline rocks and carbonatite at ~900 Ma (Fig. 13c; Mukherjee *et al.* 2018b; Das *et al.* 2019). Our study corroborates the view of Burke *et al.* (2003) that DARs/DARCs represent extensional and compressional phases of the 'Wilsonian cycle'. However, the extensional phase may or may not lead to opening of an ocean basin (as in case of CGGC); thus the DARCs along the NPSZ should not be treated as a marker for tracing ancient terrane boundaries.

7.d. Significance of the studied DARs in the context of the supercontinent cycle

It is now generally accepted that the Proterozoic Eon witnessed four major supercontinent cycles including the Superia (Sclavia), Columbia (Nuna), Rodinia and Gondwana (Brown, 2007). Extensive geochronological studies on the rocks of these supercontinents put reasonably tight constraints on the formation and breakdown phases of each of these supercontinents (Fig. 14). Paul *et al.* (2020), in their exhaustive analyses of published data on the Indian DARs/DARCs, compiled the ages of emplacement of the magmatic protoliths and the metamorphism of these rocks. We have plotted these data in Figure 14 using the following filters: (1) Only the dates that are based on U–Pb and Sm–Nd systematics are considered; this will ensure interpretation of the DARs/DARCs in the context of supercontinent cycles. (2) The age data of a few DARs/DARCs are revised in recent studies. These changes have been accommodated. The inferred age range of the DARCs in the NPSZ are also included (Das *et al.* 2019).

Corroborating the view of Burke *et al.* (2003), emplacement ages of the magmatic protoliths of practically all the DARs/DARCs coincide with the phases of supercontinent breakdown (Fig. 14). A preponderance of ARs/ARCs during the phase of breakdown of the Columbia supercontinent covering the Aravalli Craton, the Palaeoproterozoic part of the Eastern Ghats Belt, Dharwar Craton, to the Archaean Rengali Province raises the possibility that a large part of the Indian shield formed a coherent block during the formation of the Columbia supercontinent and subsequently rifted with or without the formation of an open ocean basin during Mesoproterozoic time (Fig. 14). The magmatic emplacement age of some DARs/DARCs from Koraput and Purulia (NPSZ and SPSZ) postdate the major phases of the Grenvillian orogeny (~1000–950 Ma). Mukherjee *et al.* (2018b) showed that both India and east Antarctica (Rayner Complex), which share the ~1000–950 Ma high-grade metamorphism, preserve phases of extension between ~950 and 920 Ma. Subsequently, the Indo-Antarctic land mass witnessed another phase of continent–continent collision at ~920–900 Ma (Maji *et al.* 2008; Karmakar *et al.* 2011; Sanyal & Sengupta, 2012; Chatterjee, 2018; Mukherjee *et al.* 2018b, 2019b; Das *et al.* 2019; Dey *et al.* 2019b; Olierook *et al.* 2019). Similar metamorphic ages
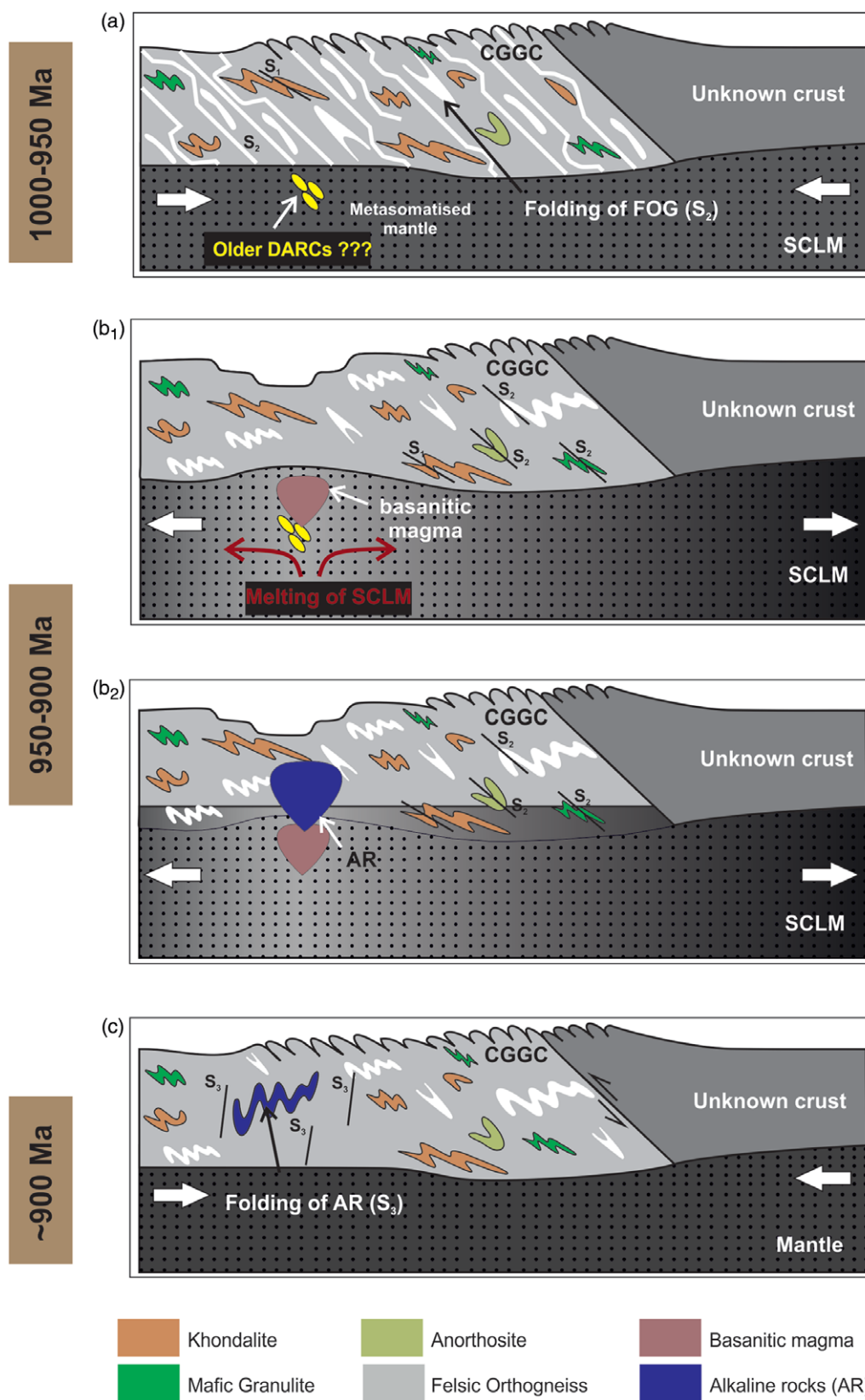
Fig. 13. (Colour online) Schematic diagram of the evolutionary model illustrating the petrogenesis of the studied deformed nepheline syenite showing the (a) formation of the high-grade rocks with the prominent S_2 fabric in a continent–continent collision at 1000–950 Ma. (b_1) Generation of a basanitic magma by low-degree partial melting of sub-continental lithospheric mantle (SCLM, compositionally garnet peridotite) in a continental rift setting. (b_2) Further crystal fractionation of clinopyroxene, apatite, ilmenite, titanite and zircon produced the nepheline syenite (blue) magma that was emplaced in the crust at 950–900 Ma. (c) Rifting failed and the nepheline syenite along with the basement it includes was deformed and metamorphosed in another continent–continent collision at ~900 Ma.
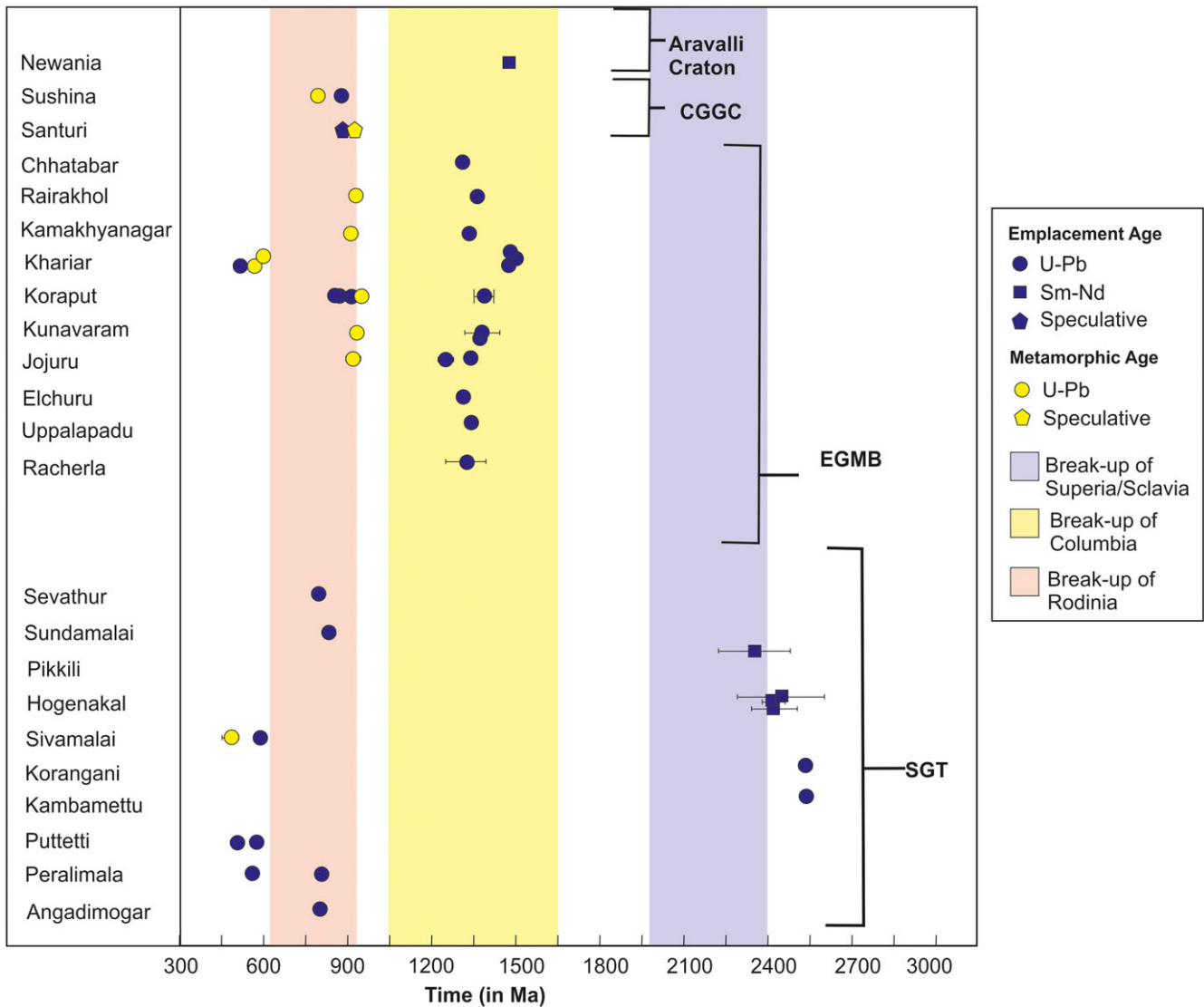
Fig. 14. (Colour online) Emplacement and metamorphic ages of Proterozoic alkaline rocks and carbonatites of India showing relationship of their emplacement and metamorphism with major supercontinent cycles. Detailed information on these localities is given in Paul *et al.* (2020).

are also recorded in the DARCs and the adjoining ~1000–950 Ma basement of Purulia (Paul *et al.* 2020 and references therein). Figure 14 demonstrates that all the metamorphic ages of the Indian DARs/DARCs coincide with the formation of the Proterozoic supercontinents. In view of the foregoing analyses, we are of the view that detailed study of the DARs/DARCs is extremely important not only to demonstrate the 'Wilsonian cycle' but also to trace the supercontinental cycles.

8. Conclusions

The main results of our study lead to the following conclusions:

(a) The ~1000–950 Ma old granulite-grade gneissic basement in the southern segment of the CGGC developed a rift zone now marked by the NPSZ during the period of 950–900 Ma.

(b) As a consequence of rifting, the metasomatized garnet peridotite of the SCLM beneath the CGGC underwent partial melting, presumably in response to the lithospheric extension.

(c) The low degree of partial melting of the SCLM produced a basanitic melt that upon fractional crystallization of clinopyroxene, ilmenite, apatite and titanite led to the generation of the studied nepheline syenite magma.

(d) Nepheline syenite magma eventually emplaced in the rift zone in the CGGC at ~800–900°C, a mid crustal depth and low fO_2 conditions (below FMQ).

(e) Extant geological information is consistent with the view that the rifting did not eventually lead to an open ocean and hence is a 'failed' rift.

(f) Subsequently, the CGGC with its nepheline syenite and carbonatite was buried under a continental block in a continent–continent collisional setting at ~900 Ma.

(g) This study corroborates the view that the Indian shield and the granulites of east Antarctica (Rayner Complex) shared a common geological history with two phases of continent–continent collisional events at ~1000–950 Ma and 920–900 Ma that are punctuated by a phase of crustal extension. The extension and compression cycle led to the formation of the DARCs of the NPSZ during the time span of ~950–900 Ma.

References

Ablay GJ, Carroll MR, Palmer MR, Marti J and Sparks RSJ (1998) Basanite–phonolite lineages of the Teide–Pico Viejo Volcanic Complex, Tenerife, Canary Islands. *Journal of Petrology* **39**, 905–36.

Acharyya SK (2003) The nature of Mesoproterozoic Central Indian Tectonic Zone with exhumed and reworked older granulites. *Gondwana Research* **6**, 197–214.

Acharyya A, Ray S, Chaudhuri BK, Basu SK, Bhaduri SK and Sanyal AK (2006) Proterozoic rock suites along South Purulia Shear Zone, Eastern India: evidence of rift related setting. *Journal of the Geological Society of India* **68**, 1069–86.

Ahmed HA, Ma C, Wang L, Palinkaš LA, Girei MB, Zhu Y and Habib M (2018) Petrogenesis and tectonic implications of peralkaline A-type granites and syenites from the Suizhou-Zaoyang Region, Central China. *Journal of Earth Science* **29**, 1181–202.

Ashwal LD, Armstrong RA, Roberts RJ, Schmitz MD, Corfu F, Hetherington CJ, Burke K and Gerber M (2007) Geochronology of zircon megacrysts from nepheline-bearing gneisses as constraints on tectonic setting: implications for resetting of the U–Pb and Lu–Hf isotopic systems. *Contributions to Mineralogy and Petrology* **153**, 389–403.

Ashwal LD, Patzelt M, Schmitz MD and Burke K (2016) Isotopic evidence for a lithospheric origin of alkaline rocks and carbonatites: an example from Southern Africa. *Canadian Journal of Earth Sciences* **53** (11), 1216–26.

Aulbach S, O'Reilly SY, Griffin WL and Pearson NJ (2008) Subcontinental lithospheric mantle origin of high niobium/tantalum ratios in eclogites. *Nature Geoscience* **1**, 468–72.

Bailey DK (1974) Origin of alkaline magmas as a result of anatexis crustal anatexis. In *The Alkaline Rocks* (ed. H Sorensen), pp. 436–42. New York: Wiley and Sons.

Bailey DK and Schairer JF (1966) The system Na_2O-Al_2O_3-Fe_2O_3-SiO_2 at 1 atmosphere, and the petrogenesis of alkaline rocks. *Journal of Petrology* **7**, 114–70.

Baker BH (1987) Outline of the petrology of the Kenya rift alkaline province. In *Alkaline Igneous Rocks* (eds JG Fitton and BGJ Upton), pp. 293–311. Geological Society of London, Special Publication no. 30.

Basu SK (1993) Alkaline-carbonatite complex in Precambrian of South Purulia Shear Zone, Eastern India: its characteristics and mineral potentialities. *Indian Minerals* **261**, 179–94.

Basu SK (2003) Petrogenetic model for evolution of Alkaline-Carbonatite Complex along Tamar-Porapahar Shear Zone in North Singhbhum Proterozoic Mobile Belt, Eastern India and its metallogenic aspects. *Journal of the Geological Society of India* **62**, 250–2.

Bell K and Blenkinsop J (1987) Nd and Sr isotopic compositions of East African carbonatites: implications for mantle heterogeneity. *Geology* **15**, 99–102.

Bell K and Simonetti A (2010) Source of parental melts to carbonatites – critical isotopic constraints. *Mineralogy and Petrology* **98**, 77–89.

Bell K and Tilton GR (2001) Nd, Pb and Sr isotopic compositions of East African carbonatites: evidence for mantle mixing and plume inhomogeneity. *Journal of Petrology* **42**, 1927–45.

Bhaumik T, Mukherjee S and Bose A (1990) Petrology of nepheline syenites from Santuri, Puruliya District, West Bengal. *Geological Society of India* **36**, 589–606.

Bhowmik SK, Wilde SA, Bhandari A, Pal T and Pant NC (2012) Growth of the Greater Indian landmass and its assembly in Rodinia: geochronological evidence from the Central Indian Tectonic Zone. *Gondwana Research* **22**, 54–72.

Bizimis M, Salters VJM and Dawson JB (2003) The brevity of carbonatite sources in the mantle: evidence from Hf isotopes. *Contributions to Mineralogy and Petrology* **145**, 281–300.

Bowen NL (1928) *The Evolution of Igneous Rocks*. Princeton: Princeton University Press, 334 pp.

Brown M (2007) Metamorphism, plate tectonics, and the supercontinent cycle. *Earth Science Frontiers* **14**, 1–18.

Burke K, Ashwal LD and Webb SJ (2003) New way to map old sutures using deformed alkaline rocks and carbonatites. *Geology* **31**, 391–4.

Burke K and Khan S (2006) Geoinformatic approach to global nepheline syenite and carbonatite distribution: testing a Wilson cycle model. *Geosphere* **2**, 53–60.

Burke K, Khan SD and Mart RW (2008) Grenville province and Monteregian carbonatite and nepheline syenite distribution related to rifting, collision, and plume passage. *Geology* **36**, 983–6.

Burke K, Roberts D and Ashwal LD (2007) Alkaline rocks and carbonatites of northwestern Russia and northern Norway: linked Wilson cycle records extending over two billion years. *Tectonics* **26**, 1–10.

Casquet C, Pankhurst RJ, Galindo C, Rapela C, Fanning CM, Baldo E, Dahlquist J, Casado JMG and Colombo F (2008) A deformed alkaline igneous rock – carbonatite complex from the Western Sierras Pampeanas, Argentina: evidence for late Neoproterozoic opening of the Clymene Ocean? *Precambrian Research* **165**, 205–20.

Castillo PR (2016) A proposed new approach and unified solution to old Pb paradoxes. *Lithos* **252–253**, 32–40.

Chakrabarty A, Mitchell RH, Ren M, Saha PK, Pal S, Pruseth KL and Sen AK (2016) Magmatic, hydrothermal and subsolidus evolution of the agpaitic nepheline syenites of the Sushina Hill Complex, India: implications for the metamorphism of peralkaline syenites. *Mineralogical Magazine* **80**, 1161–93.

Chakrabarty A and Sen AK (2010) Enigmatic association of the carbonatite and alkali-pyroxenite along the Northern Shear Zone, Purulia, West Bengal: a saga of primary magmatic carbonatite. *Journal of the Geological Society of India* **76**, 403–13.

Chakraborty S and Ganguly J (1991) Compositional zoning and cation diffusion in garnets. In *Diffusion, Atomic Ordering and Mass Transport* (ed. J Ganguly), pp. 120–75. New York: Springer-Verlag New York.

Chakraborty K, Ray A, Chatterjee A, Deb GK and Das K (2019) Neoproterozoic granitic activity in syn-collisional setting: insight from petrology, geochemistry, and zircon–monazite geochronology of S-type granites of the Chotanagpur Granite Gneissic Complex, eastern India. *Geological Journal* **54**, 3112–47.

Chalapathi Rao NV, Gibson SA, Pyle DM and Dickin AP (2004) Petrogenesis of Proterozoic lamproites and kimberlites from the Cuddapah Basin and Dharwar Craton, southern India. *Journal of Petrology* **45**, 907–48.

Chalapathi Rao NV, Giri RK and Pandey A (2020) Kimberlites, lamproites and lamprophyres from the Indian shield: highlights of researches during 2016–2019. *Proceedings of the Indian National Science Academy* **86**, 301–11.

Chalapathi Rao NV, Wu FY and Srinivas M (2012) Mesoproterozoic emplacement and enriched mantle derivation of the Racherla alkali syenite, Palaeo-Mesoproterozoic Cuddapah Basin, southern India: insights from *in situ* Sr–Nd isotopic analysis on apatite. In *Palaeoproterozoic of India* (eds R Mazumder and D Saha), pp. 185–95. Geological Society of London, Special Publication no. 365.

Chatterjee N (2018) An assembly of the Indian Shield at c. 1. 0 Ga and shearing at c. 876–784 Ma in Eastern India: insights from contrasting P-T paths, and burial and exhumation rates of metapelitic granulites. *Precambrian Research* **317**, 117–36.

Chatterjee N, Banerjee M, Bhattacharya A and Maji AK (2010) Monazite chronology, metamorphism–anatexis and tectonic relevance of the mid-Neoproterozoic Eastern Indian Tectonic Zone. *Precambrian Research* **179**, 99–120.

Chatterjee N, Crowley JL and Ghose NC (2008) Geochronology of the 1.55 Ga Bengal anorthosite and Grenvillian metamorphism in the Chotanagpur gneissic complex, eastern India. *Precambrian Research* **161**, 303–16.

Chatterjee N and Ghose NC (2011) Extensive Early Neoproterozoic high-grade metamorphism in North Chotanagpur Gneissic Complex of the Central Indian Tectonic Zone. *Gondwana Research* **20**, 362–79.

Chattopadhyay S, Upadhyay D, Nanda JK, Mezger K, Pruseth KL and Berndt J (2015) Proto-India was a part of Rodinia: evidence from Grenville-age suturing of the Eastern Ghats Province with the Paleoarchean Singhbhum Craton. *Precambrian Research* **266**, 506–29.

Cheng X, Xu J, Wei H, Yang F, Zhang H and Zhang G (2018) Petrology, geochronology and geochemistry of Late Triassic alkaline rocks of the Bailinchuan district in Liaodong Peninsula, Northeast China. *Minerals* **8**, 528. doi: 10.3390/min8110528.

Chowdhury P, Talukdar M, Sengupta P, Sanyal A and Mukhopadhyay D (2013) Controls of P-T path and element mobility on the formation of corundum pseudomorphs in Paleoproterozoic high-pressure anorthosite from Sittampundi, Tamil Nadu, India. *American Mineralogist* **98**, 1725–37.

Das S, Dasgupta N, Sanyal S, Sengupta S, Karmakar S and Sengupta P (2017) Dolomitic carbonatite from the Chotanagpur Granite Gneiss Complex: a new DARC (Deformed Alkaline Rocks and Carbonatite) in the Precambrian shield of India. *Current Science* **113**, 1038–40.

Das S, Sanyal S, Karmakar S, Sengupta S and Sengupta P (2019) Do the deformed alkaline rocks always serve as a marker of continental suture zone? A case study from parts of the Chotanagpur Granite Gneissic complex, India. *Journal of Geodynamics* **129**, 59–79.

Dasgupta S, Bose S and Das K (2013a) Tectonic evolution of the Eastern Ghats Belt, India. *Precambrian Research* **227**, 247–58.

Dasgupta R, Mallik A, Tsuno K, Withers AC, Hirth G and Hirschmann MM (2013b) Carbon-dioxide-rich silicate melt in the Earth's upper mantle. *Nature* **493**, 211–5.

Dawson JB (1987) The kimberlite clan: relationship with olivine and leucite lamproites, and inferences for upper-mantle metasomatism. In *Alkaline Igneous Rocks* (eds JG Fitton and BGJ Upton), pp. 95–102. Geological Society of London, Special Publication no. 30.

Deer WA, Howie RA and Zussman J (1962) *An Introduction to the Rock Forming Minerals*. London: Longmans, 528 pp.

Dey A, Roy Choudhury S, Mukherjee S, Sanyal S and Sengupta P (2019a) Origin of vesuvianite-garnet veins in calc-silicate rocks from part of the Chotanagpur Granite Gneiss Complex, East Indian Shield: the quantitative P–T–X CO$_2$ topology in parts of the system CaO-MgO-Al$_2$O$_3$-SiO$_2$-H$_2$O-CO$_2$ (+Fe$_2$O$_3$, F). *American Mineralogist* **104**, 744–60.

Dey A, Karmakar S, Ibanez-Mejia M, Mukherjee S, Sanyal S and Sengupta P (2019b) Petrology and geochronology of a suite of pelitic granulites from parts of the Chotanagpur Granite Gneiss Complex, eastern India: evidence for Stenian-Tonian reworking of a late Paleoproterozoic crust. *Geological Journal* **2019**, 1–30.

Dey A, Karmakar S, Mukherjee S, Sanyal S and Dutta U (2019c) High pressure metamorphism of mafic granulites from the Chotanagpur Granite Gneiss Complex, India: evidence for collisional tectonics during assembly of Rodinia. *Journal of Geodynamics* **129**, 24–43.

Dey A, Mukherjee S, Sanyal S, Ibanez-Mejia M and Sengupta P (2017) Deciphering sedimentary provenance and timing of sedimentation from a suite of metapelites from the Chotanagpur Granite Gneissic Complex, India: implications for Proterozoic tectonics in the East-Central part of the Indian Shield. In *Sediment Provenance: Influences on Compositional Change from Source to Sink* (ed. R Mazumder), pp. 453–86. Amsterdam: Elsevier.

Eby GN, Woolley AR, Din VIC and Platt G (1998) Geochemistry and petrogenesis of nepheline syenites: Kasungu–Chipala, Ilomba, and Ulindi nepheline syenite intrusions, North Nyasa Alkaline Province, Malawi. *Journal of Petrology* **39**, 1405–24.

Edgar AD (1987) The genesis of alkaline magmas with emphasis on their source regions: inferences from experimental studies. In *Alkaline Igneous Rocks* (eds JG Fitton and BGJ Upton), pp. 29–52. Geological Society of London, Special Publication no. 30.

Fitton JG (1987) The Cameroon line, West Africa: a comparison between oceanic and continental alkaline volcanism. In *Alkaline Igneous Rocks* (eds JG Fitton and BGJ Upton), pp. 273–91. Geological Society of London, Special Publication no. 30.

Ghiorso MS, Hirschmann MM and Reiners PW (2002) The pMELTS: a revision of MELTS for improved calculation of phase relations and major element partitioning related to partial melting of the mantle to 3 GPa. *Geochemistry, Geophysics, Geosystems* **3**, 1–36.

Gomes CB, Velázquez VF, Azzone RG and Paula GS (2011) Alkaline magmatism in the Amambay area, NE Paraguay: the Cerro Sarambí complex. *Journal of South American Earth Sciences* **32**, 75–95.

Goswami B and Basu SK (2013) Metamorphism of Proterozoic agpaitic nepheline syenite gneiss from North Singhbhum Mobile Belt, eastern India. *Mineralogy and Petrology* **107**, 517–38.

Goswami B and Bhattacharyya C (2008) Metamorphism of nepheline syenite gneisses from Chhotanagpur Granite Gneiss Complex, Northeastern Puruliya District, Eastern India. *Journal of the Geological Society of India* **71**, 209–13.

Goswami B and Bhattacharyya C (2010) Tectonothermal evolution of Chhotanagpur Granite Gneiss Complex from northeastern part of Puruliya District, West Bengal, Eastern India. *Indian Journal of Petroleum Geology* **80**, 41–54.

Green TH and Watson EB (1982) Crystallization of apatite in natural magmas under high pressure, hydrous conditions, with particular reference to 'orogenic' rock series. *Contributions to Mineralogy and Petrology* **79**, 96–105.

Hamilton DL (1961) Nephelines as crystallization temperature indicators. *The Journal of Geology* **69**, 321–9.

Hofmann AW, Jochum KP, Seufert M and White WM (1986) Nb and Pb in oceanic basalts: new constraints on mantle evolution. *Earth and Planetary Science Letters* **79**, 33–45.

Huang H, Niu Y, Zhao Z, Hei H and Zhu D (2011) On the enigma of Nb-Ta and Zr-Hf fractionation – a critical review. *Journal of Earth Science* **22**, 52–66.

Imeokparia EG (1981) Ba/Rb and Rb/Sr ratios as indicators of magmatic fractionation, postmagmatic alteration and mineralization – Afu Younger Granite Complex, Northern Nigeria. *Geochemical Journal* **15**, 209–19.

Irving AJ and Green DH (2008) Phase relationships of hydrous alkalic magmas at high pressures: production of nepheline hawaiitic to mugearitic liquids by amphibole-dominated fractional crystallization within the lithospheric mantle. *Journal of Petrology* **49**, 741–56.

Karmakar S, Bose S, Sarbadhikari AB and Das K (2011) Evolution of granulite enclaves and associated gneisses from Purulia, Chhotanagpur Granite Gneiss Complex, India: evidence for 990–940 Ma tectonothermal event(s) at the eastern India cratonic fringe zone. *Journal of Asian Earth Sciences* **41**, 69–88.

Kretz R (1983) Symbols for rock-forming minerals. *American Mineralogist* **68**, 277–9.

Kyle PR, Moore JA and Thirlwall MF (1992) Petrologic evolution of anorthoclase phonolite lavas at Mount Erebus, Ross Island, Antarctica. *Journal of Petrology* **33**, 849–75.

Le Bas MJ, Le Maitre RW and Woolley AR (1992) The construction of the Total Alkali-Silica chemical classification of volcanic rocks. *Mineralogy and Petrology* **46**, 1–22.

Le Maitre R (ed.) (2002) *Igneous Rocks: A Classification and Glossary of Terms: Recommendations of the International Union of Geological Sciences Subcommission on the Systematics of Igneous Rocks*. Cambridge: Cambridge University Press.

Leake BE, Woolley AR, Arps CES, Birch WD, Gilbert MC, Grice JD, Hawthorne FC, Kato A, Kisch HJ, Krivovichev VG, Linthout K, Liard J, Mandarino JA, Maresch WV, Nickel EH, Rock NMS, Schumacher JC, France DC, Stephenson NCN, Ungaretti L, Whittaker EJW and Youzhi G (1997) Nomenclature of amphiboles: report of the Subcommittee on Amphiboles of the International Mineralogical Association, Commission on New Minerals and Mineral names. *Canadian Mineralogist* **35**, 219–46.

Leelanandam C, Burke K, Ashwal LD and Webb SJ (2006) Proterozoic mountain building in Peninsular India: an analysis based primarily on alkaline rock distribution. *Geological Magazine* **143**, 195–212.

Li ZX, Bogdanova SV, Collins AS, Davidson A, De Waele B, Ernst RE, Fitzsimons ICW, Fuck RA, Gladkochub DP, Jacobs J, Karlstrom KE, Lu S, Natapov LM, Pease V, Pisarevsky SA, Thrane K and Vernikovsky V (2008) Assembly, configuration, and break-up history of Rodinia: a synthesis. *Precambrian Research* **160**, 179–210.

Liferovich RP and Mitchell RH (2006) Apatite-group minerals from nepheline syenite, Pilansberg alkaline complex, South Africa. *Mineralogical Magazine* **70**, 463–84.

Lindsley DH (1991) Oxide minerals: petrologic and magnetic significance. *Mineralogical Society of America* **25**, 509.

Lucassen F, Franz G, Romer RL, Schultz F, Dulski P and Wemmer K (2007) Pre-Cenozoic intra-plate magmatism along the Central Andes (17–34° S): composition of the mantle at an active margin. *Lithos* **99**, 312–38.

Mahadevan TM (2002) *Geology of Bihar and Jharkhand*. Bangalore: Geological Society of India.

Maji AK, Goon S, Bhattacharya A, Mishra B, Mahato S and Bernhardt HJ (2008) Proterozoic polyphase metamorphism in the Chhotanagpur Gneissic Complex (India), and implication for trans-continental Gondwanaland correlation. *Precambrian Research* **162**, 385–402.

McDonough WF and Sun S-S (1995) The composition of the Earth. *Chemical Geology* **120**, 223–53.

McKenzie D (1989) Some remarks on the movement of small melt fractions in the mantle. *Earth and Planetary Science Letters* **95**, 53–72.

Meert JG and Torsvik TH (2003) The making and unmaking of a supercontinent: Rodinia revisited. *Tectonophysics* **375**, 261–88.

Menzies M (1987) Alkaline rocks and their inclusions: a window on the Earth's interior. In *Alkaline Igneous Rocks* (eds JG Fitton and BGJ Upton), pp. 15–27. Geological Society of London, Special Publication no. 30.

Mitchell RH and Platt RG (1978) Mafic mineralogy of ferroaugite syenite from the Coldwell alkaline complex, Ontario, Canada. *Journal of Petrology* **19**, 627–51.

Mitchell RH and Platt RG (1982) Mineralogy and petrology of nepheline syenites from the Coldwell alkaline complex, Ontario, Canada. *Journal of Petrology* **23**, 186–214.

Morbidelli L, Gomes CB, Brotzu P, Acquarica SD, Garbarino C, Ruberti E and Traversa G (2000) The Pariquera Acu K-alkaline complex and southern Brazil lithospheric mantle source characteristics. *Journal of Asian Earth Sciences* **18**, 129–50.

Morimoto N (1988) Nomenclature of pyroxenes. *American Mineralogist* **73**, 1123–33.

Mukherjee S, Dey A, Ibanez-Mejia M, Sanyal S and Sengupta P (2018a) Geochemistry, U–Pb geochronology and Lu–Hf isotope systematics of a suite of ferroan (A-type) granitoids from the CGGC: evidence for Mesoproterozoic crustal extension in the east Indian shield. *Precambrian Research* **305**, 40–63.

Mukherjee S, Dey A, Sanyal S, Ibanez-Mejia M, Dutta U and Sengupta P (2017) Petrology and U–Pb geochronology of zircon in a suite of charnockitic gneisses from parts of the Chotanagpur Granite Gneiss Complex (CGGC): evidence for the reworking of a Mesoproterozoic basement during the formation of the Rodinia supercontinent. In *Crustal Evolution of India and Antarctica: The Supercontinent Connection* (eds NC Pant and S Dasgupta), pp. 197–231. Geological Society of London, Special Publication no. 457.

Mukherjee S, Dey A, Sanyal S, Ibanez-Mejia M and Sengupta P (2019a) Bulk rock and zircon geochemistry of granitoids from the Chotanagpur Granite Gneissic Complex (CGGC): implications for the late Paleoproterozoic continental arc magmatism in the East Indian Shield. *Contributions to Mineralogy and Petrology* **174**, 1–17.

Mukherjee S, Dey A, Sanyal S and Sengupta P (2018b) Tectonothermal imprints in a suite of mafic dykes from the Chotanagpur Granite Gneiss complex (CGGC), Jharkhand, India: evidence for late Tonian reworking of an early Tonian continental crust. *Lithos* **320–321**, 490–514.

Mukherjee S, Dey A, Sanyal S and Sengupta P (2019b) Proterozoic crustal evolution of the Chotanagpur Granite Gneissic Complex, Jharkhand-Bihar-West Bengal, India: current status and future prospect. In *Tectonics and Structural Geology: Indian Context* (ed. S Mukherjee), pp. 7–54. Cham: Springer International Publishing.

Newton RC (1992) Charnockitic alteration: evidence for CO_2 infiltration in granulite facies metamorphism. *Journal of Metamorphic Geology* **10**, 383–400.

Nude PM, Shervais JW, Attoh K, Vetter SK and Barton C (2009) Petrology and geochemistry of nepheline syenite and related carbonate-rich rocks in the Pan-African Dahomeyide orogen, southeastern Ghana, West Africa. *Journal of African Earth Sciences* **55**, 147–57.

Obeid MA and Lalonde AE (2013) The geochemistry and petrogenesis of the Late Cretaceous Abu Khuruq alkaline complex, Eastern Desert, Egypt. *Canadian Mineralogist* **51**, 537–58.

Olierook HKH, Clark C, Reddy SM, Mazumder R, Jourdan F and Evans NJ (2019) Evolution of the Singhbhum Craton and supracrustal provinces from age, isotopic and chemical constraints. *Earth-Science Reviews* **193**, 237–59.

Pagano DS, Galliski MA, Marquez-Zavalía MF and Colombo F (2016) Petrology and mineralogy of the La Peña igneous complex, Mendoza, Argentina: an alkaline occurrence in the Miocene magmatism of the Southern Central Andes. *Journal of South American Earth Sciences* **67**, 158–79.

Paul D, Chandra J and Halder M (2020) Proterozoic alkaline rocks and carbonatites of Peninsular India: a review. *Episodes* **43**, 249–77.

Peccerillo A and Taylor SR (1976) Geochemistry of Eocene calc-alkaline volcanic rocks from the Kastamonu area, Northern Turkey. *Contributions to Mineralogy and Petrology* **58**, 63–81.

Pfander JA, Jung S, Munker C, Stracke A and Mezger K (2012) A possible high Nb/Ta reservoir in the continental lithospheric mantle and consequences on the global Nb budget: evidence from continental basalts from Central Germany. *Geochimica et Cosmochimica Acta* **77**, 232–51.

Philpotts A and Ague J (2009) *Principles of Igneous and Metamorphic Petrology*. Cambridge: Cambridge University Press. doi: 10.1017/CBO9780511813429.

Platt RG and Woolley AR (1986) The mafic mineralogy of the peralkaline syenites and granites of the Mulanje complex, Malawi. *Mineralogical Magazine* **50**, 85–99.

Pouchou JL and Pichoir F (1984) A new model for quantitative X-ray microanalysis: I. – application to the analysis of homogeneous samples. *La Recherché Aérospatiale* **3**, 167–92.

Prelević D, Foley SF, Cvetković V and Romer RL (2004) Origin of minette by mixing of lamproite and dacite magmas in Veliki Majdan, Serbia. *Journal of Petrology* **45**, 759–92.

Price RC, Johnson RW, Gray CM and Frey FA (1985) Geochemistry of phonolites and trachytes from the summit region of Mt. Kenya. *Contributions to Mineralogy and Petrology* **89**, 394–409.

Ranjan S, Upadhyay D, Abhinay K, Pruseth KL and Nanda JK (2018) Zircon geochronology of deformed alkaline rocks along the Eastern Ghats Belt margin: India–Antarctica connection and the Enderbia continent. *Precambrian Research* **310**, 407–24.

Rao NVC, Kumar A, Sahoo S, Nanda P, Chahong N, Lehmann B and Rao KVS (2016) Petrogenesis of Mesoproterozoic lamproite dykes from the Garledinne (Banganapalle) cluster, south-western Cuddapah Basin, southern India. *Mineralogy and Petrology* **110**, 247–68.

Reddy SM, Clarke C and Mazumder R (2009) Temporal constraints on the evolution of the Singhbhum Crustal Province from U–Pb SHRIMP data. In *Paleoproterozoic Supercontinents and Global Evolution, Abstract Volume* (eds D Saha and R Mazumder), pp. 17–18. International Association for Gondwana Research Conference Series 9.

Rekha S, Upadhyay D, Bhattacharya A, Kooijman E, Goon S, Mahato S and Pant NC (2011) Lithostructural and chronological constraints for tectonic restoration of Proterozoic accretion in the Eastern Indian Precambrian shield. *Precambrian Research* **187**, 313–33.

Rogers JJW and Santosh M (2002) Configuration of Columbia, a Mesoproterozoic Supercontinent. *Gondwana Research* **5**, 5–22.

Rollinson HR (1993) *Using Geochemical Data: Evaluation, Presentation, Interpretation*. Harlow: Pearson Education Ltd.

Rossi G, Oberti R and Smith DC (1989) The crystal structure of a K-poor Ca-rich silicate with the nepheline framework, and crystal-chemical relationships in the compositional space (K,Na,Ca,D)8(Al,Si)16O32. *European Journal of Mineralogy* **1**, 59–70.

Sanyal S and Sengupta P (2012) Metamorphic evolution of the Chotanagpur Granite Gneiss Complex of the East Indian Shield: current status. In

Palaeoproterozoic of India (eds R Mazumder and D Saha), pp. 117–45. Geological Society of London, Special Publication no. 365.

Sarkar T and Schenk V (2016) Early Mesoproterozoic (1.6–1.5 Ga) granulite-facies events in the Ongole domain: geodynamic significance and global correlation. *Journal of Metamorphic Geology* **34**, 765–84.

Sengupta P, Dasgupta S, Bhattacharya PK and Mukherjee M (1990) An orthopyroxene–biotite geothermometer and its application in crustal granulites and mantle-derived rocks. *Journal of Metamorphic Geology* **8**, 191–7.

Sengupta P, Raith MM, Kooijman E, Talukdar M, Chowdhury P, Sanyal S, Mezger K and Mukhopadhyay D (2015) Provenance, timing of sedimentation and metamorphism of metasedimentary rock suites from the Southern Granulite Terrane, India. In *Precambrian Basins of India: Stratigraphic and Tectonic Context* (eds R Mazumder and PG Eriksson), pp. 297–308. Geological Society of London, Memoirs no. 43.

Shand SJ (1943) *Eruptive Rocks: Their Genesis, Composition, Classification, and Their Relation to Ore-Deposits, with a Chapter on Meteorites*, 2nd Edition. New York: John Wiley & Sons, 444 pp.

Sharma A, Kumar A, Pankaj P, Pandit D, Chakrabarti R and Rao NVC (2019) Petrology and Sr–Nd isotope systematics of the Ahobil kimberlite (Pipe-16) from the Wajrakarur field, Eastern Dharwar craton, southern India. *Geoscience Frontiers* **10**, 1167–86.

Smith PM and Asimow PD (2005) Adiabat_1ph: a new public front-end to the MELTS, pMELTS, and pHMELTS models. *Geochemistry, Geophysics, Geosystems* **6**, 1–8.

Thompson RN (1974) Some high-pressure pyroxenes. *Mineralogical Magazine* **39**, 768–87.

Tilley CE (1954) Nepheline-alkali feldspar parageneses. *American Journal of Science* **252**, 65–751.

Touret JLR, Newton RC and Cuney M (2019) Incipient charnockites from southern India: the role of brines. *Geoscience Frontiers* **10**, 1789–801.

Upadhyay D (2008) Alkaline magmatism along the southeastern margin of the Indian shield: implications for regional geodynamics and constraints on craton-Eastern Ghats Belt suturing. *Precambrian Research* **162**, 59–69.

Upadhyay D, Jahn-Awe S, Pin C, Paquette JL and Braun I (2006a) Neoproterozoic alkaline magmatism at Sivamalai, southern India. *Gondwana Research* **10**, 156–66.

Upadhyay D and Raith MM (2006) Petrogenesis of the Kunavaram alkaline complex and the tectonothermal evolution of the neighboring Eastern Ghats Belt granulites, SE India. *Precambrian Research* **150**, 73–94.

Upadhyay D, Raith MM, Mezger K, Bhattacharya A and Kinny PD (2006b) Mesoproterozoic rifting and Pan-African continental collision in SE India: evidence from the Khariar alkaline complex. *Contributions to Mineralogy and Petrology* **151**, 434–56.

Upadhyay D, Raith MM, Mezger K and Hammerschmidt K (2006c) Mesoproterozoic rift-related alkaline magmatism at Elchuru, Prakasam Alkaline Province, SE India. *Lithos* **89**, 447–77.

Viana RR and Battilani GA (2014) SHRIMP U–Pb and U–Pb laser ablation geochronological on zircons from Monte Santo alkaline intrusive suite, Western Araguaia Belt, Tocantins State, Brazil. *Journal of Geoscience and Environment Protection* **2**, 170–80.

Wones DR (1989) Significance of the assemblage titanite + magnetite + quartz in granitic rocks. *American Mineralogist* **74**, 744–9.

Woolley AR (2001) *Alkaline Rocks and Carbonatites of the World: Africa*. London: Geological Society of London, 366 pp.

Woolley AR, Platt RG and Eby GN (1996) Relatively aluminous alkali pyroxene in nepheline syenites from Malawi: mineralogical response to metamorphism in alkaline rocks. *Canadian Mineralogist* **34**, 423–34.

Woolley AR, Williams CT, Wall F, Garcia D and Moutez J (1995) The Bingo carbonatite-ijolite-nepheline syenite complex, Zaire: geology, petrography, mineralogy and petrochemistry. *Journal of African Earth Sciences* **21**, 329–48.

Zappettini EO, Villar LM, Hernández LB and Santos JO (2013) Geochemical and isotopic constraints on the petrogenesis of the Puesto La Peña undersaturated potassic complex, Mendoza province, Argentina: geodynamic implications. *Lithos* **162–163**, 301–16.

Zhang S, Li Z, Evans DAD, Wu H, Li H and Dong J (2012) Pre-Rodinia supercontinent Nuna shaping up: a global synthesis with new paleomagnetic results from North China. *Earth and Planetary Science Letters* **353–354**, 145–55.

Zhao JX, Shiraishi K, Ellis DJ and Sheraton JW (1995) Geochemical and isotopic studies of syenites from the Yamato Mountains, East Antarctica: implications for the origin of syenitic magmas. *Geochimica et Cosmochimica Acta* **59**, 1363–82.